catalysts

MDPI

Article

Surface-Controlled Photo-Fenton Activity of Cu-Fe Bimetallic Catalysts: Dual Function of Iron on Silica and Alumina Supports

Nimisha Kuruvangattu Puthenveettil [1,2], Goran Dražić [1], Albin Pintar [1,*] and Nataša Novak Tušar [1,3]

[1] National Institute of Chemistry, Hajdrihova ulica 19, SI-1001 Ljubljana, Slovenia; nimisha.kuruvangattu.puthenveettil@ki.si (N.K.P.); goran.drazic@ki.si (G.D.); natasa.novak.tusar@ki.si (N.N.T.)
[2] Faculty of Chemistry and Chemical Technology, University of Ljubljana, Večna pot 113, SI-1000 Ljubljana, Slovenia
[3] Graduate School, University of Nova Gorica, Vipavska cesta 13, SI-5000 Nova Gorica, Slovenia
* Correspondence: albin.pintar@ki.si; Tel.: +386-1-47-60-237

Abstract

Photo-Fenton advanced oxidation processes are promising and sustainable approaches for water treatment, particularly under visible-light irradiation. In this study, Cu-Fe bimetallic catalysts supported on silica and γ-alumina were developed for visible-light-driven photo-Fenton reactions, with emphasis on the influence of metal ratios and support-metal interactions on charge–carrier dynamics and hydroxyl radical formation. Comprehensive characterization (XRD, TEM, UV-Vis DRS, PL, TCSPC, and EPR) revealed stronger metal–support interactions and higher metal dispersion on γ-alumina, while silica-supported catalysts showed CuO aggregation at higher Cu loadings. Catalytic performance was evaluated using coumarin oxidation as both a model reaction and a quantitative probe for $^{\bullet}$OH radical generation. Alumina-supported catalysts exhibited superior activity, and $^{\bullet}$OH production increased with increasing Cu content on both supports. Importantly, iron was found to play a dual role: low Fe loading enhances photo-Fenton activity, whereas higher Fe content promotes charge–carrier recombination, leading to reduced activity under visible-light irradiation. These results highlight how the interplay between Fe/Cu ratio and support material governs charge dynamics and provides clear guidelines for the rational design of efficient heterogeneous photo-Fenton catalysts.

Keywords: photo-Fenton reaction; Cu-Fe bimetallic catalysts; silica (SiO_2) and alumina (Al_2O_3) supports; heterogeneous photocatalysis; visible-light activation; water treatment

1. Introduction

The influx of contaminants of emerging concern (CECs), such as pharmaceuticals and personal care products (PPCPs), into water bodies is one of the main causes of aquatic system degradation [1,2]. Advanced oxidation processes (AOPs) include various innovative and sustainable treatment technologies that utilize highly reactive oxygen species, especially hydroxyl radicals ($^{\bullet}$OH), which are widely used to degrade organic contaminants in water and provide an environmentally friendly solution to environmental problems [3–5]. The Fenton process, which belongs to the AOP and is based on the Fe-assisted decomposition of hydrogen peroxide (H_2O_2) into $^{\bullet}$OH, is extensively studied due to its high effectiveness and applicability [6,7]. The operational efficiency and sustainability of the homogeneous Fenton process can be improved by developing heterogeneous Fenton-like systems by addressing its drawbacks, such as the need for acidic pH (with a preferred pH range of 2.8–3.5), high

Academic Editor: Sebastiano Campisi

Received: 10 November 2025
Revised: 19 December 2025
Accepted: 22 December 2025
Published: 1 January 2026

https://doi.org/10.3390/catal16010034

chemical consumption, formation of iron sludge, leaching of iron, etc. Researchers around the world are looking for ways to transform Fenton catalysis into an efficient, affordable, and sustainable means of water treatment by overcoming the prevailing challenges in the field [8–10].

In the endeavor to develop efficient Fenton catalysts, various aspects of the catalysts and the catalytic process have been investigated. A large number of studies were carried out to develop the most successful version of the Fenton catalyst. These studies focused on the catalyst design [11–13], the catalytic mechanism [10,14], the operating conditions [15,16], the stability and reusability of the catalyst [17–19], and the potential application areas [9,13,20]. Subsequently, Fenton catalysts evolved into various subcategories, such as homogeneous Fenton [21], heterogeneous Fenton [22], photo-Fenton [11,23], electro-Fenton [24,25], sono-Fenton [26,27], and so on. If we look at the wide landscape of Fenton catalysts, a variety of materials, their modifications, or combinations are used as catalysts. These materials mainly include various iron oxides, spinels, and perovskites containing iron or iron minerals such as magnetite, hematite, maghemite, ferrihydrite, etc. [28–31]. These minerals have also been used in combination with plasmonic materials [32], metal oxides [33,34], carbon nanotubes [35], graphene oxide [36,37], MXenes [38], g-C_3N_4 [39] etc. Fenton catalysts with heterojunctions have also received much attention in recent years [40,41]. Zero valent iron [42,43], zero valent copper [44], complexes of iron and copper [45,46], metal–organic frameworks (MOFs) [47,48], metal-free catalysts made of graphene [49], activated carbon [50], and supported Fenton-like catalysts [23,51] are the latest trends in Fenton research. Understanding the mechanism of Fenton catalysis is also a priority, and each stage of Fenton catalysis is being thoroughly investigated [52,53]. From a sustainable and economic point of view, the development of highly stable and reusable catalysts is of great importance. Over the years, research in the field of Fenton catalysts has explored new areas of application and is still inventing new catalytic formulations.

As we aim to design and develop sustainable and affordable water treatment strategies, we can always utilize the enormous potential of solar energy. By combining the abundance of sunlight with the excellent properties of Fenton-like catalysis, photo-Fenton catalysts can be produced. The utilization of visible light as an energy source (photo-Fenton) allows for milder reaction conditions (neutral pH), superior H_2O_2 activation, and environmental friendliness in contrast to classical Fenton reactions [54,55]. These systems can be modified further to perform better by incorporating transition metals (e.g., Cr, Co, Mn, and Cu) into the Fenton catalysts [50,53]. Cu stands out among these as it can contribute to fast Cu^+/Cu^{2+} redox cycling, producing more reactive oxygen species and enhancing Fe-driven H_2O_2 activation under visible light. The unique chemical composition of iron-based transition metal complexes makes them structurally rigid, hence avoiding secondary pollution by the metal leaching into the solution during degradation reactions. The efficiency, stability, and reusability can be further enhanced by providing adequate catalytic support and by optimizing metal concentrations within multicomponent Fenton catalysts [56,57]. Despite several investigations on Cu-Fe systems, the combined effects of adjusted Cu/Fe ratios and varied supports on metal dispersion, electronic structure, and photo-Fenton performance at neutral pH remain poorly understood. This limits the development of catalysts that are more stable and active.

To improve the Fenton catalysis for efficient pollutant degradation, we explored a bimetallic approach along with influential catalyst supports. The incorporation of Cu into the Fe salts accelerates $^\bullet OH$ radical generation in more moderate environments due to the synergistic effects arising from the redox interplay between these transition metals. In our study, mesoporous silica (neutral support) was employed as one of the supports because it offers high surface area, thermal stability, and durability [58,59]. γ-alumina prepared from dawsonite precursor was chosen as another promising support due to its acid-base properties and strong metal–support interactions [60–62]. Cu-Fe catalysts supported on silica and alumina were selected, as our group has investigated them previously for comparable applications [63,64]. In those studies, the redox synergy and structural stability of Cu-Fe systems for Fenton-type reactions were explored; the fundamental roles of support chemistry, metal dispersion, and Fe/Cu ratios in governing photo-driven reactivity remained insufficiently understood. Building on these findings, the present work represents a conceptual extension of our prior research, wherein we systematically vary metal loadings and employ two distinct supports (silica and γ-alumina) to explicitly unravel how support-metal interactions and Fe content influence charge separation, $^{\bullet}$OH radical generation, and visible-light photo-Fenton performance. Furthermore, despite being widely employed supports, the effects of silica and γ-alumina on Cu-Fe speciation in photo-Fenton catalysis have rarely been explicitly compared. The main scientific question this work attempts to answer is how adjusting Cu/Fe molar ratios in conjunction with two structurally distinct supports impacts charge transfer behavior, $^{\bullet}$OH radical production, and light-assisted activity.

Therefore, this study attempts to address this gap by methodically investigating the effect of (i) Cu/Fe ratio and (ii) support chemistry (silica vs. γ-alumina) on the structural, electronic, and catalytic properties of bimetallic Cu-Fe photo-Fenton catalysts. We focus on developing bimetallic Cu-Fe photo-Fenton-like catalysts supported on silica and alumina, with systematically varied metal ratios, to study the influence of support interaction and metal dispersion on the structural, physicochemical, and catalytic properties. Fe was incorporated into the supports at a molar ratio of 0.005 (Fe/Al or Fe/Si), while Cu was loaded at varying molar ratios of 0.005, 0.01, and 0.02 (Cu/Al or Cu/Si). Silica-based Cu-Fe catalysts were prepared by direct synthesis followed by calcination, while alumina-based Cu-Fe catalysts were prepared from an ammonium dawsonite precursor followed by wet impregnation and calcination. The influence of supports and metal ratios on catalyst properties, including phase formation, porosity, elemental distribution, their valence oxidation states, and electronic properties, was investigated through comprehensive characterization using XRD, N_2 physisorption, SEM-EDX, TEM, UV-Vis DRS, PL, TCSPC, and EPR techniques. The catalysts were evaluated for their efficiency in their Fenton-like and photo-Fenton-like activity by monitoring the generation of hydroxyl radicals using coumarin as a fluorescence probe. In addition, as a component of pharmaceutical and personal care products (PPCPs), coumarin contributes to water pollution and represents a worldwide environmental issue [65].

2. Results and Discussion

2.1. Catalyst Characterization

2.1.1. X-Ray Diffraction (XRD) Analysis

Figure 1 shows the XRD patterns of synthesized Cu-Fe bimetallic catalysts having fixed Fe content and varying Cu contents distributed over silica and alumina supports. All the obtained XRD patterns show amorphous character, along with mesoporous nature. The mesoporous nature of the silica-supported catalysts is identical to that of the catalysts developed by Wang et al. [66]. The crystallographic character and mesoporous properties of the alumina-supported bimetallic catalysts are in agreement with the findings reported by Huang et al. [67]. The XRD profiles also show the nanometer-size distribution of the developed catalyst compositions. Figure 1a shows the XRD profiles of Cu-Fe bimetallic catalyst compositions developed by choosing three different Cu/Si ratios while maintaining a constant Fe/Si ratio. For silica-supported catalyst samples, with an increase in Cu loading, the X-ray diffraction peaks corresponding to CuO are becoming more prominent, which points to the formation of CuO nanocrystallites over the silica support. The average crystallite size was estimated using the Scherrer equation based on the width of the CuO diffraction peaks, and the results are listed in Table 1.

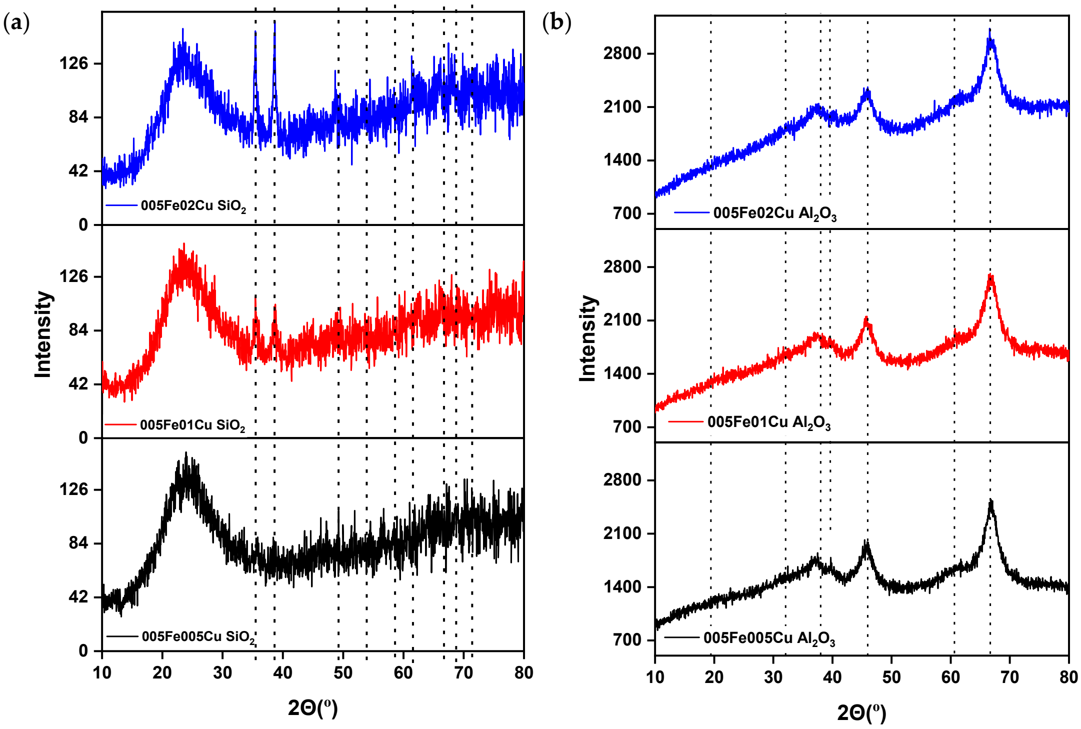

Figure 1. XRD patterns of Cu-Fe bimetallic catalysts with constant Fe/Si and Fe/Al molar ratios and increasing Cu content, supported on (**a**) silica and (**b**) alumina. Dotted lines indicate reference pattern of CuO (JCPDS: 00-001-1117) in (**a**) and γ-Al_2O_3 (00-029-0063 JCPDS) in (**b**).

Table 1. Crystallite sizes of CuO determined from X-ray diffraction data using Scherrer equation.

Catalyst	Crystallite Size (nm)
005Fe005Cu SiO_2	-
005Fe01Cu SiO_2	12.1
005Fe02Cu SiO_2	20

XRD patterns of Cu-Fe bimetallic compositions with different Cu/Al ratios and a constant Fe/Al ratio on alumina are shown in Figure 1b. Here, the γ-alumina phase was confirmed, but no distinct metal oxide diffraction peaks were observed, indicating that the metal components are in a highly dispersed state. The dispersion of Cu is therefore better on an alumina support than on silica. There is no evidence of distinct FeO_x phases in either the silica or alumina-supported catalyst variants. Although no CuO peaks are observed, Scherrer analysis of the γ-Al_2O_3 peaks indicates average crystallite sizes of 3.80–4.38 nm (Table 2), confirming the crystalline nature of the alumina support and supporting high dispersion of Cu species.

Table 2. Crystallite sizes of γ-Al_2O_3 determined from X-ray diffraction data using Scherrer equation.

Catalyst	Crystallite Size (nm)
005Fe005Cu Al_2O_3	4.36
005Fe01Cu Al_2O_3	3.80
005Fe02Cu Al_2O_3	4.38

2.1.2. Scanning Electron Microscopy and Energy-Dispersive X-Ray Spectroscopy (SEM-EDX) Analysis

The elemental compositions of the synthesized Cu-Fe bimetallic catalysts were determined by energy-dispersive X-ray spectroscopy (EDX). The EDX analysis confirmed the presence of oxygen, silicon, aluminum, iron, and copper as the main constituents of the developed bimetallic catalysts. Elemental mapping was performed on multiple regions of each catalyst sample to confirm homogeneity. The average values from these regions were then used to calculate the reported molar Fe/Si and Cu/Si ratios, ensuring that the ratios represent the overall surface composition rather than localized variations. The Fe/Si and Cu/Si ratios calculated from the atomic percentages of Fe, Cu, and Si are listed in Table 3. The results of SEM-EDX analysis show that the actual Fe loading in the synthesized Cu-Fe bimetallic catalysts on both supports is close to the expected molar ratio of 0.005. As for Cu loading, the alumina-supported bimetallic catalysts are in better agreement with the nominal stoichiometric Cu/Si ratio. The local formation of CuO nanocrystallites on the silica support leads to higher Cu/Si ratios. In the catalysts with the alumina support, both Cu and Fe are evenly distributed over the support.

Table 3. Elemental composition and molar ratios of synthesized samples obtained from SEM-EDX analysis.

Catalyst	Fe/Si	Cu/Si	Fe/Al	Cu/Al
005Fe005Cu SiO_2	0.007	0.01	-	-
005Fe01Cu SiO_2	0.007	0.02	-	-
005Fe02Cu SiO_2	0.007	0.04	-	-
005Fe005Cu Al_2O_3	-	-	0.007	0.01
005Fe01Cu Al_2O_3	-	-	0.006	0.01
005Fe02Cu Al_2O_3	-	-	0.007	0.02

Due to possible surface segregation, accurate metal quantification is particularly important for silica-supported Cu-Fe catalysts. As SEM-EDX provides only semiquantitative data, ICP-OES analysis was performed (Table S1). The results show a nearly constant Fe/Si ratio, indicating uniform Fe incorporation, while the Cu/Si ratio increases with Cu content, in agreement with the intended loading. Table S1 also shows good agreement between the nominal and actual loading for alumina-supported Cu-Fe catalysts.

2.1.3. Nitrogen Physisorption and BET Surface Area Analysis

N_2 adsorption–desorption isotherms of the developed Cu-Fe bimetallic catalysts are given in Figure 2. Specific surface area, total pore volume, and average pore sizes of the synthesized catalysts were estimated from adsorption–desorption isotherms and are summarized in Table 4. N_2 adsorption–desorption isotherms of both silica-supported and alumina-supported Cu-Fe bimetallic catalysts exhibit type IV adsorption isotherms with H1 hysteresis. The type IV adsorption–desorption isotherms indicate the mesoporous nature of the synthesized catalysts, while H1 hysteresis is characteristic of the narrow range of uniform mesopores [68]. The surface properties of the bimetallic catalysts on silica supports and the variation of the surface area with metal loading are similar to those reported by Wang et al. [66]. The porous character of the developed alumina-supported bimetallic catalysts is consistent with literature data [69]. Importantly, the silica-supported catalysts exhibit substantially higher BET surface areas than the alumina-supported ones, which can be attributed to the intrinsically more open and amorphous mesoporous structure of silica that generally preserves its porosity more effectively during metal incorporation and calcination. In contrast, γ-Al_2O_3 is known to undergo partial pore shrinkage and densification upon impregnation and thermal treatment, and its stronger interactions with Cu and Fe precursors may lead to partial pore blockage [69]. These effects are likely responsible for the lower accessible surface area observed for the alumina-supported catalysts. Despite the lower surface area, alumina-supported Cu-Fe bimetallic catalysts exhibit superior Cu dispersion, and a gradual decrease in surface area with increasing Cu loading is observed, which can also be associated with an increase in pore size arising from the enhanced density of surface defects generated upon Cu incorporation [70].

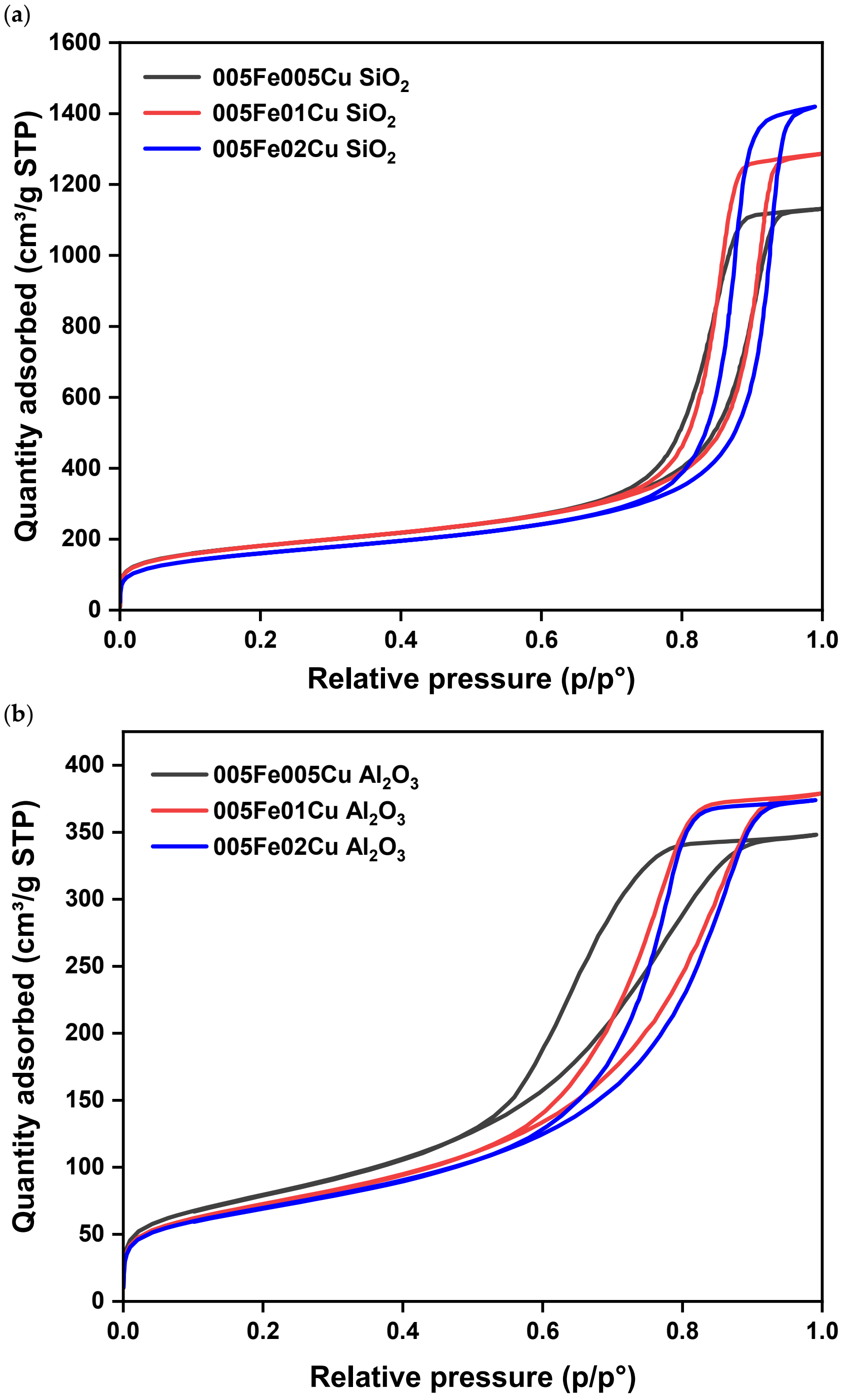

Figure 2. N_2 adsorption–desorption isotherms of Cu-Fe bimetallic catalysts supported on (**a**) SiO_2 and (**b**) Al_2O_3.

Table 4. Textural properties (surface area, pore volume, and average pore size) of Cu-Fe catalysts supported on silica and alumina.

Catalyst	S_{BET} (m^2/g)	V_{pore} at p/p° = 0.98 (cm^3/g)	Average Pore Size (nm)
005Fe005Cu SiO_2	650	1.75	18.8
005Fe01Cu SiO_2	654	1.98	21.3
005Fe02Cu SiO_2	611	2.19	24.8
005Fe005Cu Al_2O_3	286	0.55	5.3
005Fe01Cu Al_2O_3	258	0.59	6.8
005Fe02Cu Al_2O_3	247	0.59	7.3

The pore size distribution curves (dV/dW) of the silica and alumina-supported catalysts are provided in the Supplementary Information (Figure S5).

2.1.4. Transmission Electron Microscopy (TEM) Analysis

To gain a better insight into the particle morphology, crystal structure, and elemental distribution, a series of samples was selected from the prepared silica- and alumina-supported catalysts and subjected to TEM analysis. The TEM images of the best performing catalysts, i.e., 005Fe02Cu SiO_2 and 005Fe02Cu Al_2O_3, are shown in Figures 3a and 3b, respectively.

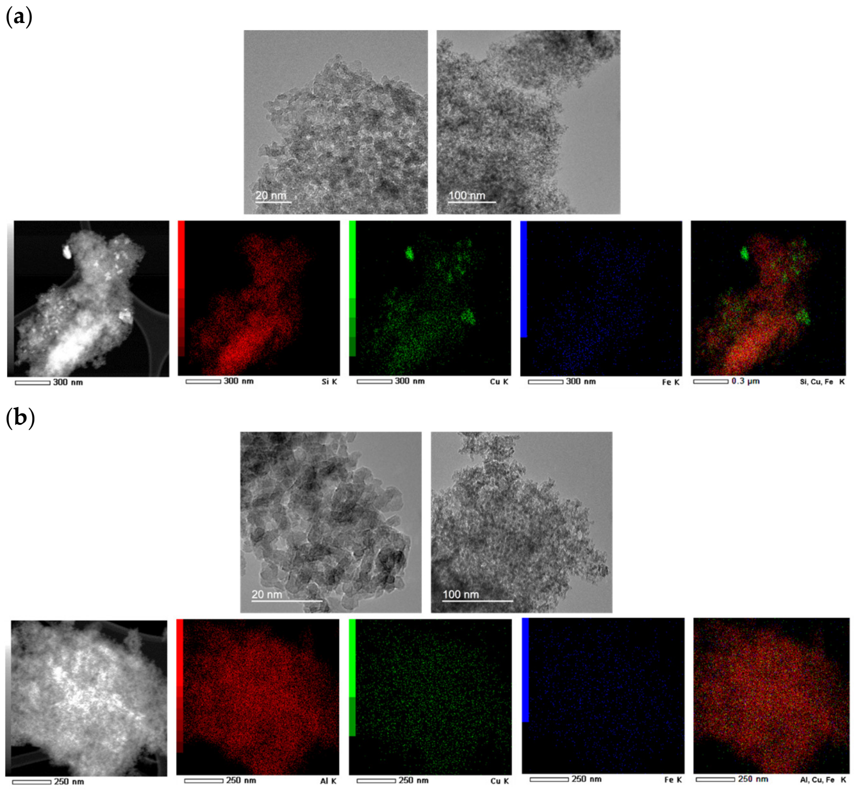

Figure 3. TEM micrographs and elemental mappings of (**a**) 005Fe02Cu SiO_2 and (**b**) 005Fe02Cu Al_2O_3 samples.

The TEM images of the 005Fe02Cu SiO_2 and 005Fe02Cu Al_2O_3 samples show uniformly sized, highly porous particles with a size of less than 10 nm. As shown in Figure S1, all the alumina-supported catalysts were uniformly dispersed, and the samples with lower copper loading in the silica-supported catalysts (005Fe005Cu SiO_2 and 005Fe01Cu SiO_2) showed uniform dispersion of elements Fe and Cu without aggregation. The elemental mapping obtained from STEM-EDXS analysis shows the presence of CuO nanoparticles in the silica-supported catalyst with the highest Cu loading (Figure 3a); the CuO nanoparticles exhibit a broad size distribution, with an average equivalent spherical diameter of 26 nm and a standard deviation of 19 nm (26 ± 19 nm), indicating significant polydispersity. This indicates a heterogeneity of Cu loading on the silica support and implies that the synthesis conditions for the composition of the catalysts on silica supports need to be further optimized. The TEM images of the 005Fe02Cu Al_2O_3 catalyst show a high degree of uniform distribution of Cu on the alumina support (Figure 3b). The SAED (Selected Area Electron Diffraction) patterns obtained from the TEM show that alumina is predominantly present in the γ-Al_2O_3 phase; however, small amounts of α-Al_2O_3 and amorphous phases are also evident. The diffuse nature of the SAED patterns indicates the amorphous nature of the silica-supported catalysts (Figure S2).

All samples with the alumina support showed a homogeneous distribution of metals throughout the support, indicating that the metal ions are well dispersed at the nanoscale and do not form larger aggregates. The existence of nanoclusters consisting of a few Cu and/or Fe atoms cannot be ruled out. Furthermore, the uniform distribution of Cu and Fe in the sample can only be explained by the existence of single atoms or few-atoms clusters. Unfortunately, imaging at the atomic level was not possible due to the sample thickness and localized charging, as SiO_2 and Al_2O_3 have a very high electrical resistance. The interactions between metal and support are better when there is a uniform distribution, which is essential to maximize the catalytic performance.

2.1.5. UV-Vis Diffuse Reflectance Spectroscopy (DRS)

The UV-Vis diffuse reflectance (DR) spectra of the synthesized Cu-Fe bimetallic catalysts are shown in Figure 4. The UV-Vis DR spectra obtained are consistent with the available literature [69,71,72]. The UV-Vis DR spectra of both silica- and alumina-supported Cu-Fe bimetallic catalysts exhibit an increase in visible-light absorption with increased Cu loading. The enhancement in visible-light absorption of the synthesized catalysts indicates their potential for photo-Fenton activity. The absorption signal observed around ~750 nm can be attributed to the d-d transitions of Cu^{2+} ions coordinated in distorted octahedral fields of oxygen ligands [58]. For all the synthesized catalyst compositions, the high energy region of the spectra (200–300 nm) can be assigned to ligand-to-metal charge transfer ($M \longleftarrow O$ CT) from O^{2-} to Fe^{3+} and Cu^{2+} ions [73–75].

On the other hand, if we compare the UV-Vis DR spectra of silica- and alumina-supported catalysts, we can observe that the catalysts with the alumina support show red-shifted (0.20–0.42 eV) absorption profiles in contrast to the catalysts with the silica support. This red-shift could indicate an enhanced photo-Fenton activity of the alumina-supported catalyst compositions and can be assumed as a result of the better dispersion of the Cu and Fe species on the alumina support and the resulting improved interaction between the support and the active metal species, which favors better charge transfer.

The optical band gaps of the synthesized catalysts were evaluated from Tauc plots derived from DRS data (Figure 5, Table 5), corresponding to the absorption onset and assuming direct electronic transitions. This choice of a direct bandgap is justified because CuO nanoparticles are known to exhibit direct transitions, providing a more accurate estimation of their visible-light absorption properties. The catalysts exhibited direct band gaps in the range of 3.3–3.8 eV, which are comparable to or slightly lower than values reported in previous studies [76,77].

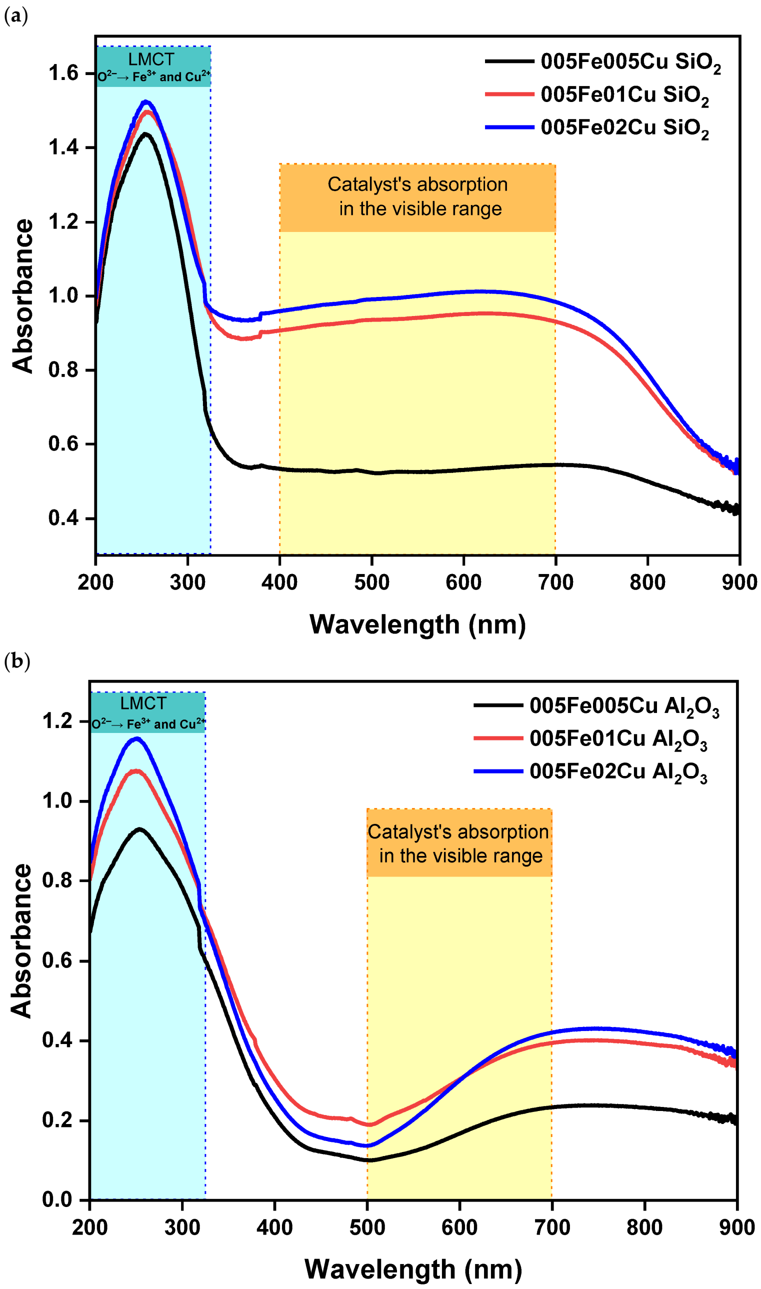

Figure 4. UV-Vis DR spectra of Cu-Fe bimetallic catalysts with fixed Fe content and variable Cu loading supported on (**a**) SiO_2 and (**b**) Al_2O_3.

Table 5. Band gap values of the catalysts determined from Tauc plots.

Sample	Bandgap (eV)
005Fe005Cu SiO_2	3.76
005Fe01Cu SiO_2	3.56
005Fe02Cu SiO_2	3.62
005Fe005Cu Al_2O_3	3.34
005Fe01Cu Al_2O_3	3.42
005Fe02Cu Al_2O_3	3.52

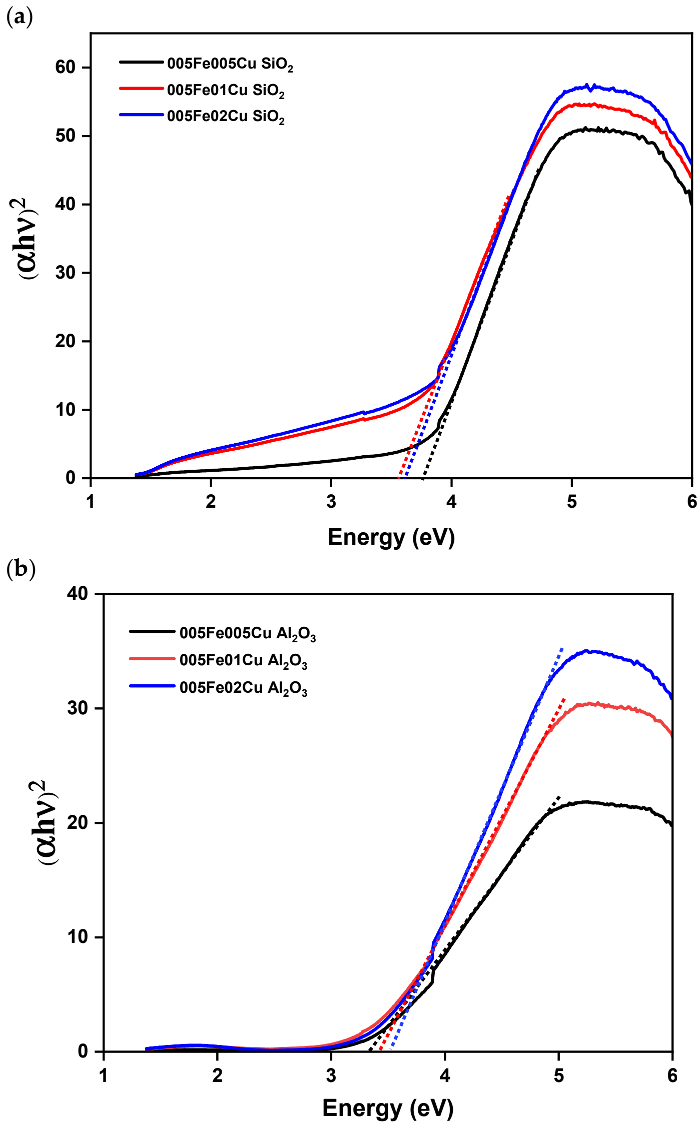

Figure 5. Tauc plots derived from UV-Vis DRS data for Cu-Fe bimetallic catalysts with varying Cu content on (**a**) SiO_2 and (**b**) Al_2O_3.

2.1.6. Photoluminescence (PL) Analysis

The fluorescence spectra of Cu-Fe bimetallic catalysts supported on SiO_2 and Al_2O_3 were recorded at excitation wavelengths of 240 nm and 450 nm (Figure 6). A strong emission peak around 400 nm is observed under UV excitation (240 nm) with a very small peak at ~300 nm, in all samples (Figure 6a,b). The ligand-to-metal charge transfer (LMCT) transitions involving $O^{2-} \rightarrow Fe^{3+}$ and Cu^{2+} interactions as well as emission from surface defects (oxygen vacancies, integrated metal ions, etc.) can be attributed to the peak at ~400 nm, while the much weaker peak at ~300 nm is due to emission induced by bulk defects [78,79]. The absolute intensities of bulk and surface defects (oxygen vacancies) are comparable for silica- and alumina-based catalysts. When normalized to the specific surface area, alumina-based catalysts show a significantly higher defect density than silica-based catalysts, indicating a higher concentration of active defect sites per unit area (Table S2). A higher number of surface defects improves the dispersion of the metal species and the catalytic activity by enhancing the interactions between the metal carriers in the alumina-based catalysts (see below).

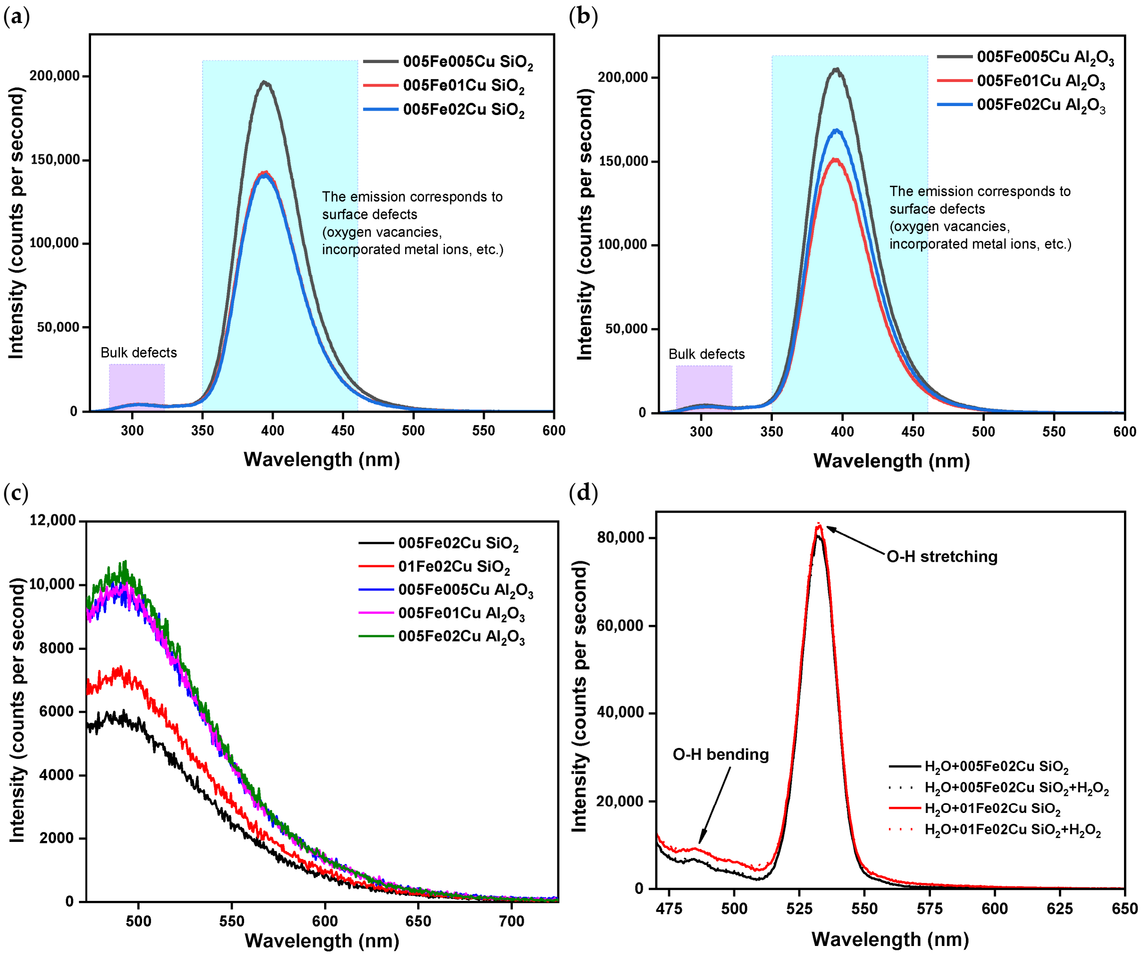

Figure 6. Photoluminescence solid-state spectra of Cu-Fe bimetallic catalysts supported on (**a**) SiO_2 and (**b**) Al_2O_3 under 240 nm excitation, (**c**) emission spectra under 450 nm excitation, and (**d**) liquid-phase PL behavior of catalysts.

PL spectral deconvolution was employed to estimate the surface-defect concentrations, including non-bridging oxygen hole center (NBOHC) emission and oxygen-vacancy recombination components (Table S3). Alumina-supported catalysts generally exhibit higher defect-related emissions than silica-supported ones, which correlates with increased charge–carrier recombination and influences photo-Fenton activity. For illustration, deconvoluted PL spectra of 005Fe02Cu SiO_2 and 005Fe02Cu Al_2O_3 samples are shown in Figure S6.

The broad emissions in the range of 470–700 nm under excitation with visible light (450 nm) in the investigation of the photo-Fenton performance of the catalysts studied are characteristic of d-d transitions of Fe^{3+} and Cu^{2+} ions (Figure 6c) and are confirmed by earlier work [77,80]. This emission is also associated with oxygen vacancies and defect states, which can act as charge–carrier trapping sites. For silica-supported catalysts with varying Fe loading and the highest Cu loading (i.e., 005Fe02Cu SiO_2 and 01Fe02Cu SiO_2 samples), excitation at 450 nm importantly reveals that the catalyst with low iron loading exhibits lower PL intensity, indicating better charge separation and enhanced production of $^{\bullet}OH$ radicals, crucial for degrading organic pollutants in wastewater.

To further verify the fluorescence emission behavior of these catalysts (005Fe02Cu SiO_2 and 01Fe02Cu SiO_2) observed in the PL spectra in the solid state, PL measurements were performed in liquid phase with water as medium (Figure 6d). Both the catalyst dispersed in water and the catalyst-water and H_2O_2 mixtures were analyzed using this technique. The PL spectra in the liquid phase showed similar responses to the PL spectra in the solid state, confirming the reproducibility of the emission behavior. At the same time, characteristic vibrational bands of water molecules, originating from O-H stretching and O-H bending modes, appeared in the spectra. When comparing the PL spectra in solid and liquid phases, it becomes clear that the PL emissions in both solid and liquid environments originate from the same active species, which underlines the reliability and consistency of the emission behavior in different phases. Based on the above, it is confirmed that the 01Fe02Cu SiO_2 catalyst exhibits faster regeneration of charge carriers than the 005Fe02Cu SiO_2 sample even in the liquid phase (i.e., under the conditions of the catalytic tests).

These results correlate very well with the lifetime of photogenerated electrons in the examined catalysts, as provided in Table 6, determined from the TCSPC technique, showing shorter lifetimes for higher iron loading. Overall, the lifetime of photogenerated electrons in the synthesized catalysts is less than 1 ns and needs optimization for highly active visible-light-driven photo-Fenton applications.

Table 6. TCSPC lifetime parameters of Cu-Fe bimetallic catalysts.

Sample	τ_1 (ns)	τ_2 (ns)	A_1 (%)	A_2 (%)	$\tau_{average}$ (ns)	χ^2
005Fe005Cu Al_2O_3	0.51	3.90	99.6	0.4	0.52	1.14
005Fe01Cu Al_2O_3	0.87	1.81	99.5	0.5	0.87	1.22
005Fe02Cu Al_2O_3	0.68	2.00	99.7	0.3	0.68	1.13
005Fe02Cu SiO_2	0.66	1.79	99.5	0.5	0.67	1.15
01Fe02Cu SiO_2	0.48	1.75	99.6	0.4	0.49	1.20

Note: PL decay curves were fitted with a two-exponential function and deconvoluted with an instrument response function.

2.1.7. Electron Paramagnetic Resonance (EPR) Spectroscopy

EPR spectroscopic analysis of the synthesized Cu-Fe bimetallic catalysts was carried out to understand the valence states, metal–support interactions, and extent of metal species dispersion. EPR spectra confirmed the presence of paramagnetic Fe^{3+} and Cu^{2+} species in both silica and alumina-supported bimetallic catalysts synthesized (Figure 7a,b). This is in line with expectations, taking into account the catalyst preparation procedures (calcination in air). No signals indicative of Fe^{2+} are observed in the samples [81]. The absence of signals in the EPR spectra of pure SiO_2 and Al_2O_3 without Fe and Cu components indicate the absence of paramagnetic impurities in both supports (Figure S3).

For alumina-supported catalysts, the Fe^{3+} ions exhibit a high-spin state (S = 5/2) signal (~156 mT) at around $g \approx 4.3$, which is typical for isolated high-spin Fe^{3+} in a rhombically distorted environment, and arises from the transition between $m_s = -1/2$ and $m_s = +1/2$ spin states [82]. A comparable peak is seen in the silica-supported catalysts, with a little leftward shift and a more broadened character associated with heterogeneity of the local environments of Fe^{3+}, which results from the amorphous nature of SiO_2 [81].

The intensity of EPR spectra of both silica- and alumina-supported Cu-Fe bimetallic catalysts increases with increased Cu loading, indicating enhanced paramagnetic behavior. Cu^{2+} ions are identified through their $g \approx 2.1$ (260–320 mT) resonance with hyperfine splitting for alumina-based materials. The alumina-supported catalysts exhibit partially resolved hyperfine splitting in the $g\|$ region, with three evident peaks, indicating the presence of Cu^{2+} in a semi-ordered coordination environment [83]. The broad and asymmetric nature of the peak is likely due to the heterogeneous crystal environment caused by the mixture of γ-Al_2O_3 and α-Al_2O_3 phases, which are evident from the TEM results. The absence of well-defined hyperfine splitting suggests that the parallel component is not fully resolved due to interactions with the Fe_2O_3-Al_2O_3. In contrast, the Cu^{2+} signal on silica appears as a single broadband (275–325 mT) without resolved hyperfine structure, implying a more disordered local environment or greater variation in Cu^{2+} coordination geometry caused by the amorphous SiO_2 matrix and its interactions with Fe_2O_3. Larger CuO nanoparticles on the silica support may also be the cause of the absence of hyperfine splitting [84,85]. Increasing Cu concentration leads to an enhancement of the Cu^{2+} signal, suggesting efficient substitution in the matrix. The variation in signal intensity and broadness suggests different degrees of metal dispersion and interaction [86]. However, the above-described EPR results confirm that stronger metal–support interactions are present in alumina-based catalysts than in silica-based materials.

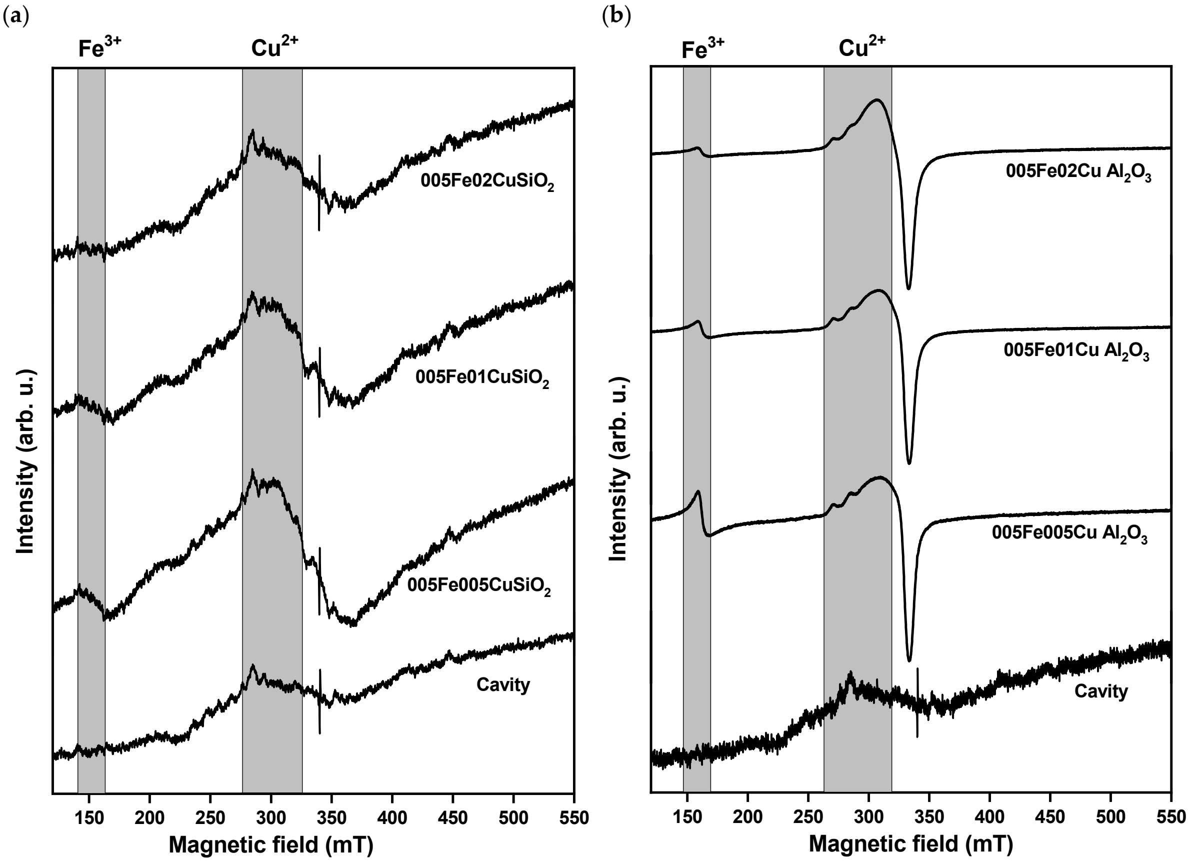

Figure 7. X-band CW EPR spectra of Cu-Fe bimetallic catalysts with increasing Cu/Si or Cu/Al molar ratios supported on (**a**) silica, and (**b**) alumina, measured at 25 °C. Cavity background curve is shown for reference.

When the samples were illuminated with visible light during EPR analysis, slight shifts and shape changes of some peaks were observed in the silica- and alumina-based catalysts with the lowest iron content, indicating the trapping of excited electrons (Figure S4). This is consistent with the results of the photo-Fenton tests, which showed the positive effect of visible-light illumination on the catalytic activity measured using coumarin as a photoluminescence probe. However, no significant changes were observed in the EPR spectra when the 01Fe02Cu SiO_2 sample (higher iron content) was illuminated with visible light during EPR analysis. This observation is consistent with the results of the PL analysis (Figure 6c) and the photo-Fenton tests performed on catalysts supported on silica, where the illumination of the reaction suspension with visible light did not increase but decreased the activity.

2.2. *Evaluation of Fenton-like and Photo-Fenton-like Catalysis Using Coumarin*

2.2.1. Catalytic Tests

The Fenton-like and photo-Fenton-like catalytic activities of the synthesized Cu-Fe bimetallic catalysts were investigated using coumarin as a photoluminescent probe.

Coumarin reacts with $^{\bullet}$OH radicals to yield 7-OHC, a fluorescent product [87]. The incorporation of H_2O_2 into the reaction medium facilitates the decomposition of H_2O_2 into highly reactive $^{\bullet}$OH radicals. These generated radicals then react with coumarin to yield 7-OHC. This conversion of coumarin to 7-OHC is a reliable indicator for determining the extent of $^{\bullet}$OH radicals formed during the reaction, which is directly linked to the catalytic efficiency in AOPs [88].

Catalytic tests were performed under dark (Fenton activity) and visible-light conditions (photo-Fenton). The pH of the reaction solution was monitored before and after each experiment. For all Cu-Fe catalysts, the initial pH was 6.0 and remained unchanged (final pH = 6.0), indicating stable reaction conditions during catalytic tests. The formation of the hydroxylated product was monitored by fluorescence spectroscopy. PL intensity was recorded at various reaction intervals for each catalyst, and the results were plotted to visualize the kinetics of $^{\bullet}$OH radical generation.

Essential control experiments were performed under the same conditions as the catalytic tests (450 nm LED, 25 °C, N_2 atmosphere, identical coumarin concentration) to distinguish photolytic, photocatalytic, and dark Fenton contributions. The controls listed below were carried out: (i) light + H_2O_2 + coumarin (no catalyst), (ii) catalyst + coumarin (no H_2O_2), and (iii) H_2O_2 + catalyst + coumarin (dark). The first two controls showed very weak 7-OHC emission, indicating negligible $^{\bullet}$OH generation from photolysis or catalyst excitation alone. In contrast, the third control showed a measurable increase in 7-OHC intensity, confirming that dark Fenton activity occurs when the catalyst reacts with H_2O_2. Figure S7 in the Supplementary Information displays the graph showing control experiments using Cu-Fe catalysts on silica and alumina supports.

Variations in PL intensity around 450 nm at different time intervals for the developed catalyst samples are shown in Figure 8, which gives quantitative information on the formation of $^{\bullet}$OH radicals and thereby a measure of catalytic activity. The full set of calculated and normalized reaction rate values is provided in the Supplementary Information (Table S4).

The coumarin tests were first conducted using the monometallic species on the Al_2O_3 support (005Fe Al_2O_3 and 01Cu Al_2O_3 samples) to understand the role of individual metal species in the reactions under consideration. Figure 8a shows the catalytic activity of Fe-only and Cu-only incorporated catalyst samples, along with a summation of the individual component activities given in comparison with the corresponding bimetallic catalyst composition. Thus, we have a clear indication of the synergistic effect of Cu and Fe species together over the alumina support. Cu-Fe bimetallic catalysts showed the highest Fenton-like activity due to synergistic effects between copper and iron, which promote better charge–carrier separation, more efficient light absorption, and improved catalytic performance [89,90].

The catalytic efficiency of Cu-Fe bimetallic solids, with a fixed Fe/Si or Fe/Al molar ratio of 0.005 and three different Cu/Si or Cu/Al ratios, i.e., 0.005, 0.01, and 0.02, was evaluated and is shown in Figure 8b,c. The catalytic study shows that alumina-supported catalysts exhibit higher catalytic activity under both dark and visible-light conditions. The catalytic activity varies significantly depending on the support material, regardless of identical metal ratios. This variation in catalytic efficiency is correlated to the strong metal–support interactions and better dispersion of metal species over alumina-supported samples than silica-based solids, even though silica exhibits a higher surface area (Table 4). The improved efficiency of alumina-supported catalysts may also be shaped by their surface acidity, which helps in the activation of the reactants [91,92]. A gradual rise in the activity was observed for both supports with higher Cu content, which can be explained based on the greater availability of active CuO sites and potential synergistic effects between

Fe- and Cu-containing phases in the bimetallic system. As can be seen in Figure 8c, the PL intensity, which corresponds to the formation of 7-OHC, increases proportionally to the Cu loading in the first part of the reaction course; this is due to the high dispersion of the active phases, as confirmed by TEM analysis. Even though the alumina-supported catalysts exhibit higher overall activity, the activity under visible-light irradiation was not appreciably improved. This subtle enhancement in activity is likely due to inefficient visible-light absorption and rapid recombination of photogenerated charge carriers, which exhibit rather short lifetimes as obtained from the TCSPC analysis (Table 6). Alternative approaches like bandgap engineering, incorporation of plasmonic materials, etc., can be employed to boost the visible-light response of these systems [93,94].

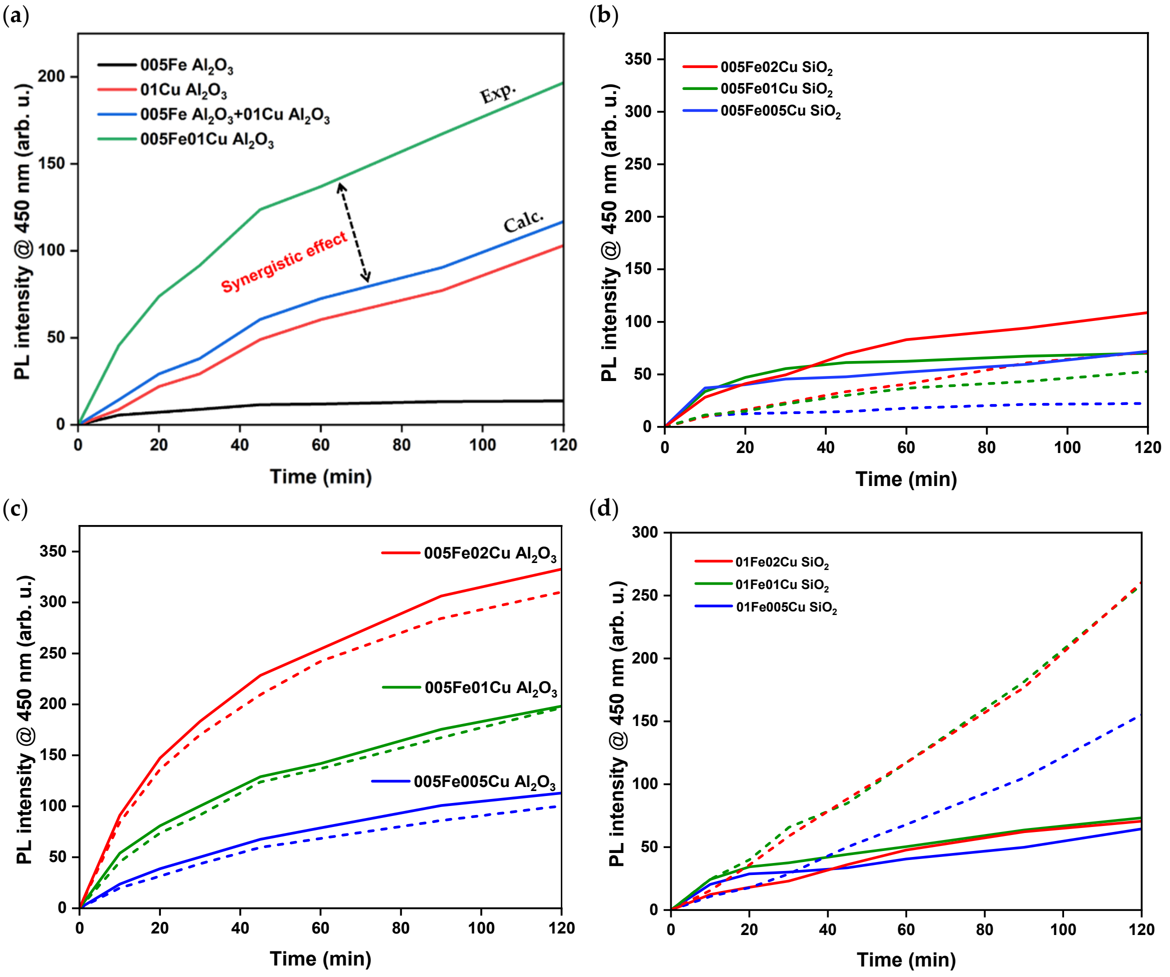

Figure 8. Photoluminescence (PL) intensity at λ = 450 nm as a function of reaction time (0–120 min) for coumarin oxidation in the presence of various Cu–Fe bimetallic catalysts under dark conditions (dotted lines) and visible-light irradiation (solid lines). (**a**) Comparative performance of single-metal (Cu-only and Fe-only) and bimetallic (Cu–Fe) catalysts on alumina support. (**b**) silica-supported Cu–Fe catalyst with a molar ratio of Fe/Si = 0.005; (**c**) alumina-supported Cu–Fe catalyst with Fe/Al = 0.005; (**d**) silica-supported Cu–Fe catalyst with Fe/Si = 0.01. PL intensity corresponds to formation of 7-hydroxycoumarin, which serves as a fluorescent probe for hydroxyl radical ($^\bullet$OH) generation in Fenton and photo-Fenton reactions.

When the Fe/Si molar ratio was increased to 0.01, the Fenton activity was significantly increased compared to the 0.005 Fe/Si catalysts, but an unexpected decrease occurred in the photo-Fenton activity (Figure 8d). This inverse response is an indication of the effect of metal loading on catalytic performance. An increase in Fe content promotes metal aggregation, reduces surface dispersion, and decreases the number of photoactive sites, thereby limiting the effective utilization of visible light and reducing the generation of $^{\bullet}$OH generation.

The assessments of PL emission spectra (Figure 6c) and TCSPC measurements of catalysts (Table 6) with higher iron loading (01Fe02Cu SiO_2) and lower iron loading (005Fe02Cu SiO_2) disclosed that the 0.01 Fe/Si catalyst exhibited a more intense PL emission peak (in both solid-state and liquid-phase measurements) and shorter lifetime compared to the 0.005 Fe/Si catalyst, implying that the higher iron content leads to faster recombination of photogenerated charge carriers. In other words, an increased iron content (most likely in the form of Fe_2O_3) leads to a higher surface concentration of Fe^{3+}, but at the same time impairs photogeneration and charge separation. It might be also speculated that the fast recombination observed in PL and TCSPC measurements can be attributed to the formation of small FeO_x clusters on the silica surface, acting as electron traps. As a result, there is an increased electron–hole recombination (e^-/h^+), which reduces the probability of Fe^{3+} being reduced to Fe^{2+}. Since Fe^{2+} is the active species responsible for the generation of $^{\bullet}$OH radicals, the photo-Fenton activity decreases (schematically illustrated in Figure 9, right panel). In contrast, at lower iron loading (Figure 9, left panel), reduced recombination losses allow more efficient electron transfer via CuO-related states, facilitating Fe^{3+}/Fe^{2+} redox cycling and sustained $^{\bullet}$OH radical formation under visible-light irradiation. Although CuO could in principle still facilitate the formation of $^{\bullet}$OH radicals under illumination, the dominant negative effects of the iron-containing oxides—through increased recombination, physical coverage of the CuO sites, and formation of electron traps—outweigh the positive contribution of CuO. Consequently, a net decrease in activity can be observed in Figure 8d under illumination with visible light [90,91].

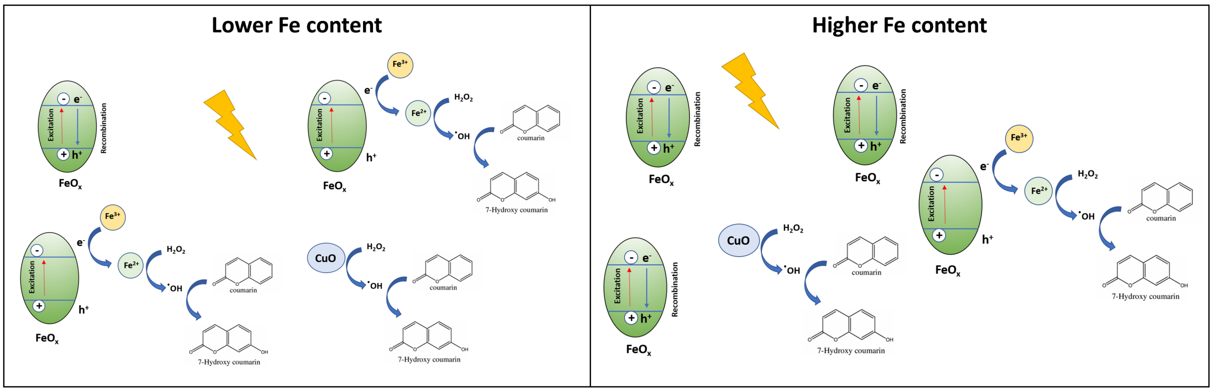

Figure 9. Proposed photo-Fenton mechanism of Cu-Fe bimetallic catalysts under visible-light irradiation. Illumination generates photogenerated electrons and holes, which participate in CuO-mediated charge transfer and accelerate Fe^{3+}/Fe^{2+} redox cycling. At low Fe loading, efficient charge separation promotes regeneration of Fe^{2+}, which reacts with H_2O_2 to produce hydroxyl radicals ($^{\bullet}$OH) responsible for selective oxidation of coumarin to 7-hydroxycoumarin (7-OHC). At higher Fe content, increased charge–carrier recombination limits Fe^{2+} regeneration and suppresses photo-Fenton activity. The schematic summarizes the interplay between charge–carrier dynamics, Cu-Fe synergistic interactions, hydroxyl radical generation, and the observed catalytic performance.

To verify the structural stability of the catalysts after the catalytic tests, post-reaction XRD and TEM analyses were performed. The XRD patterns before and after reaction display identical phase compositions, with only a slight decrease in peak intensity, indicating minor leaching but no structural changes. TEM images further confirm the structural stability by retaining their morphology and dispersion: CuO domains remain present in the spent 005Fe02Cu SiO_2 catalyst, consistent with the fresh sample, while the 005Fe02Cu Al_2O_3 catalyst maintains uniformly dispersed metal species after reaction. Post-reaction XRD and TEM data of 005Fe02Cu SiO_2 and 005Fe02Cu Al_2O_3 samples are provided in the Supplementary Information (Figures S8 and S9).

2.2.2. Metal Leaching Analysis

The metal leaching tests of the prepared catalyst compositions were performed under Fenton reaction conditions to examine the stability and ecological integrity of the prepared materials using the ICP-MS technique. Leaching measurements of all the synthesized catalysts were carried out under the same operating and reaction conditions to ensure the reliability and coherence of the experimental results. A 20 mM solution of 30% H_2O_2 was introduced into 100 mL of an aqueous solution containing 40 mg of a photocatalyst, and the mixture was stirred for four hours. Followed by 4 h of agitating the suspension at 300 rpm, the aqueous-phase samples were extracted, promptly filtered through a 0.2 µm membrane filter, and then analyzed. The ICP-MS method offers high sensitivity for trace metal detection with a detection limit of 0.5 µg/L. Leaching concentrations obtained from the analysis were compared against the permissible limits outlined in the European Drinking Water Directive (Council Directive 98/83/EC), which specifies maximum permissible concentrations of 2000 µg/L for Cu (Annex I, page 36) and 200 µg/L for Fe (page 40).

All the catalysts proved their excellent structural integrity, resulting from minimal leaching well below the regulatory limits under oxidative stress (Table 7). The low leaching values refer to the eco-friendliness of the materials and their importance in sustainable water treatment applications. The minor differences in leaching concentration between materials supported by silica and alumina are probably due to variations in the metal–support interaction. Alumina-supported catalysts had relatively lower leaching values than their silica counterparts, because of their stronger ability to anchor metals, suggesting that the support material plays a significant role in heterogeneous catalysis.

Table 7. Measured concentrations of leached metals after catalytic treatment (ICP-MS).

Catalyst	Cu (µg/L)	Fe (µg/L)
005Fe005Cu SiO_2	264	6
005Fe01Cu SiO_2	185	1
005Fe02Cu SiO_2	267	3
01Fe005Cu SiO_2	213	15
01Fe01Cu SiO_2	258	19
01Fe02Cu SiO_2	462	17
005Fe005Cu Al_2O_3	83	2
005Fe01Cu Al_2O_3	462	1
005Fe02Cu Al_2O_3	733	<1

3. Experimental

3.1. Chemicals

Tetraethylammonium hydroxide (TEAOH, 35 wt.%, Sigma-Aldrich, Saint Louis, MO, USA), tetraethyl orthosilicate (TEOS, 98%, Sigma-Aldrich), triethanolamine (TEA, 99%, Sigma-Aldrich), copper(II) acetate monohydrate ($Cu(CH_3COO)_2 \cdot H_2O$, 98%, Aldrich), iron(III) chloride hexahydrate ($FeCl_3 \cdot 6H_2O$, 98%, Sigma-Aldrich), aluminum chloride hexahydrate ($AlCl_3 \cdot 6H_2O$, Sigma-Aldrich), and ammonium carbonate ($(NH_4)_2CO_3$, Sigma-Aldrich) were obtained from Sigma-Aldrich (St. Louis, MO, USA) and used without further purification. Copper(II) nitrate trihydrate ($Cu(NO_3)_2 \cdot 3H_2O$, 99–104%, Honeywell Fluka) was purchased from Honeywell Fluka (Buchs, Switzerland). Coumarin ($C_9H_6O_2$, 98%, Alfa Aesar, Ward Hill, MA, USA) was used as a model organic pollutant and a probe for

$^{\bullet}$OH radical detection. Ultrapure water (18.2 MΩ·cm, Type 1) was used throughout the synthesis to ensure high-purity conditions.

3.2. Preparation of Catalysts

3.2.1. Preparation of Silica-Supported Catalysts

Bimetallic Cu-Fe functionalized silica-supported catalysts were prepared using a previously reported synthesis procedure for mesoporous silica KIL [95]. In the first step, 25 g of silica source, tetraethyl orthosilicate (TEOS, Sigma-Aldrich, 98%), was combined with copper acetate monohydrate ($Cu(CH_3COO)_2 \cdot H_2O$, Sigma-Aldrich, 98%) in varying amounts to achieve the theoretical molar ratios of Cu/Si = 0.005, 0.01, and 0.02 and stirred for 10 min. Iron (III) chloride hexahydrate ($FeCl_3 \cdot 6H_2O$, Sigma-Aldrich) was then added to obtain the theoretical molar ratio of Fe/Si = 0.005, and the mixture was stirred for 10 min. Triethanolamine (TEA, 8.86 g, Sigma-Aldrich (St. Louis, MO, USA), 99%) as a structure-directing agent (directs the polycondensation of silicate species) and ultrapure water were added and stirred for another 30 min. After 30 min of continuous stirring, tetraethylammonium hydroxide (TEAOH, 8.66 g, Sigma-Aldrich, 35 wt.%) was added as a pH moderator, and continuous stirring was applied to obtain a homogeneous gel. The pH of the gel after addition of TEAOH was around 11, which facilitated homogeneous polycondensation of silicate species. The formed gel was aged overnight at room temperature and then dried in a furnace for 24 h at 50 °C. In the second step, the gel was thoroughly ground and subjected to a solvothermal treatment in ethanol for 48 h at 150 °C in a Teflon-lined stainless-steel autoclave. After multiple decants, the solid product was washed with ethanol. With a calcination step at 500 °C for 10 h, the template was extracted from the pores at a 10 °C/min ramp rate under continuous airflow. During overnight aging and solvothermal treatment, the pH gradually stabilized without significant fluctuations.

The synthesized materials were denoted as 005Fe005Cu SiO_2, 005Fe01Cu SiO_2, and 005Fe02Cu SiO_2.

3.2.2. Preparation of Alumina-Supported Catalysts

In this study, a two-step synthesis method was used to create Cu-Fe-modified alumina supports from an ammonium dawsonite ($NH_4AlCO_3(OH)_2$) precursor with constant Fe loading (Fe/Al = 0.005) and variable Cu loading (Cu/Al = 0.005, 0.01, and 0.02). The synthesis procedure followed previously reported data in [96,97], with a few modifications such as changing the molar ratios between the compounds and switching from nitrate to chloride in the case of the Fe precursor, as described by Žumbar et al. [64].

In the first step (Al_2O_3 synthesis and in situ iron incorporation), ammonium aluminum carbonate hydroxide was made by mixing ammonium carbonate solution (2 M, $(NH_4)_2CO_3$, Sigma-Aldrich) and aluminum chloride hexahydrate solution (2 M, $AlCl_3 \cdot 6H_2O$, Sigma-Aldrich) in a molar ratio of 4:1 in favor of the basic compound. To achieve the required Fe/Al molar ratio of 0.005 in the calcined aluminum oxide, iron was added to the neutralization reaction in a volume of 1 mL using a 0.15 M iron(III) chloride hexahydrate ($FeCl_3 \cdot 6H_2O$, 98%, Sigma-Aldrich) solution. A peristaltic pump was used to introduce the ingredients, and the flow was adjusted to maintain a pH of 7.75–8.25 during the neutralization reaction, ensuring controlled dawsonite formation and preventing boehmite formation. The suspension was then heated to 85 °C in an oil bath and vigorously stirred for three hours. Ultrapure water was used to filter and wash the product. The water to Al_2O_3 mass ratio was 30:1 to avoid the unwanted production of boehmite [96,97]. After washing, the dawsonite was dried at 105 °C for 24 h. The substance was subsequently calcined for two hours at 700 °C in the presence of air to produce γ-alumina from the dawsonite structure. The pH remained stable during heating at 85 °C for 3 h and subsequent drying and calcination.

In the final step, copper was deposited by the incipient wetness impregnation method with 0.2 M copper(II) nitrate trihydrate ($Cu(NO_3)_2{\cdot}3H_2O$, 99–104%, Honeywell Fluka, Buchs, Switzerland) solution to obtain the necessary Cu/Al molar ratios of 0.005, 0.01, and 0.02 in the calcined aluminum oxide. Following the successful impregnation, the samples were calcined for an hour at 500 °C after being dried overnight.

The synthesized materials were denoted as 005Fe005Cu Al_2O_3, 005Fe01Cu Al_2O_3, and 005Fe02Cu Al_2O_3.

3.3. Materials Characterization

X-ray powder diffraction (XRD) was employed to analyze the structural characteristics of the synthesized materials. Diffractograms were recorded using a PANalytical (Almelo, The Netherlands) X′Pert PRO high-resolution diffractometer with Cu $K\alpha_1$ radiation (λ = 0.15406 nm), operating at 40 kV and 30 mA at ambient conditions between 10 and 70° 2Θ for silica-supported catalysts and 5 and 80° 2Θ for alumina-supported catalysts with a step of 0.034° and 100 s per step.

The distribution of the elements on the catalyst surface was analyzed using energy-dispersive X-ray spectroscopy (EDX) connected to a field emission scanning electron microscope (FE-SEM, Zeiss Supra 35VP, Carl Zeiss, Oberkochen, Germany) with an INCA 400 EDXS system (Oxford Instruments, Abingdon, UK). The EDX measurements were performed under high vacuum conditions with an accelerating voltage of 20 keV and an aperture of 30 µm.

The textural characteristics, such as specific surface area, total pore volume, and average pore size, were determined from nitrogen adsorption–desorption isotherms recorded on a Micromeritics (Norcross, GA, USA) Tristar II 3020 device at −196 °C. The samples were degassed sequentially for 1 h at 90 °C and 3 h at 200 °C. For silica-based catalysts, the Brunauer–Emmett–Teller (BET) specific surface area was estimated from adsorption data in the relative pressure range from 0.06 to 0.165 [98], while for alumina-based samples, it was measured from 0.05 to 0.30 [68]. The total pore volume was calculated at a relative pressure of 0.98 [99]. The Barrett, Joyner, and Halenda (BJH) technique was used to compute the pore size distributions (PSDs) from nitrogen adsorption–desorption data [100].

Ultraviolet-visible (UV-Vis) diffuse reflectance (DR) spectra of the synthesized samples were measured on a Perkin Elmer (Waltham, MA, USA) Lambda 650 UV-VIS spectrophotometer equipped with a Praying Mantis accessory from Harrick (Pleasantville, NY, USA). Samples were scanned in the spectral range between 200 and 900 nm, with a slit set to 4 nm and a scanning speed of 140 nm min^{-1}. Spectralon® was used as the reference for the background correction.

The morphology, particle size of the derived materials, the presence of iron and copper, and nanoparticles of oxides in the silica or alumina matrix were studied using High-Resolution Scanning Transmission Electron Microscopy (HR-STEM). The analysis was conducted on a Cs probe-corrected STEM (ARM 200 CF, JEOL Ltd., Tokyo, Japan) equipped with a dual-EELS system (Quantum ER, Gatan, Pleasanton, CA, USA), and a Centurio energy-dispersive X-ray spectroscopy (EDXS) system featuring a 100 mm^2 silicon drift detector (JEOL Ltd., Tokyo, Japan). For TEM investigations, a drop of sample dispersion diluted with ethanol was put on a nickel grid coated with lacey carbon and allowed to dry at room temperature. Bright-field (BF) imaging and high-angle annular dark-field (HAADF) imaging were the two observation methods employed in the STEM mode.

The Horiba (Kyoto, Japan) Fluorolog-QM 75-22-C spectrofluorometer, equipped with a CW 75 W Xe light source, double monochromators and a cooled 920 PMT detector, was used to record the solid-state photoluminescence (PL) spectra of the materials as well as the PL spectra of the aqueous suspensions of the analyzed materials at the excitation wavelengths of 240 nm and 450 nm (excitation and emission slits set to 8 nm, step size 0.5 nm, integration 1 s, ranges 260–600 nm and 470–720 nm). The fluorescence lifetime measurements of the analyzed materials were performed with the same device using time-correlated single photon counting (TCSPC) with a DeltaDiode 495 nm laser light as pulsed excitation source. For the TCSPC measurements, a picosecond photon detector (Horiba, model PPD 850) was used instead of the PMT detector. A Ludox SM-30 solution of colloidal silica was used as a reference to determine the instrument response function (IRF), which was used to calculate the lifetimes of the charge carriers with the FelixFL spectroscopy software (Horiba, version 1.0.48.0). The Ludox solution is ideally suited for this purpose due to its fast light scattering and negligible fluorescence, ensuring accurate measurement of the system's response over time. Based on the measured instrument response function, the temporal resolution of the applied TCSPC configuration (including the pulsed light source, detector, and timing electronics) allows reliable measurement of fluorescence lifetimes greater than 18 ps.

An Adani (Minsk, Belarus) CMS 8400 EPR spectrometer was used to acquire solid-state CW X-band electron paramagnetic resonance (EPR) spectra at room temperature. A quartz sample tube was filled with powder samples, which were then put into the EPR spectrometer (9.4 MHz microwave frequency). Measurements at room temperature were centered at 338.00 mT (sweep width 450 mT), with a mod. amplitude of 450 µT and a power attenuation of 15 dB (gain value of 3×10^3). An average value for one spectrum was obtained by taking three consecutive measurements for 360 s. EPR spectra were also collected by illuminating the examined samples using visible light (Schott, Mainz, Germany, model KL 2500 LED) via the EPR spectrometer's side channel.

The presence of residual and leached metals, including Cu and Fe, was analyzed in the aqueous samples using inductively coupled plasma-optical emission spectrometry (ICP-OES, Varian (Palo Alto, CA, USA), model 715-ES).

3.4. Catalytic Evaluation of Hydroxyl Radical Generation Using Coumarin as a Probe

The coumarin test is commonly used to detect the generation of $^\bullet$OH radicals during Fenton-like reactions by the synthesized catalysts. In this study, coumarin serves both as a model organic pollutant and as a probe molecule, reacting with $^\bullet$OH radicals to produce a fluorescent product, 7-hydroxycoumarin (7-OHC). The photoluminescence method was employed to quantify $^\bullet$OH radical formation in the presence of the catalysts. The reaction parameters, including catalyst dose, coumarin concentration, stirring rate, H_2O_2 concentration, and pH (~6), were chosen based on previously reported optimized conditions to ensure efficient and reproducible $^\bullet$OH radical generation [101]. A glass double-wall batch slurry reactor from Lenz Laborglas was used for the measurements (Figure S10). A mass of 20 mg of a photocatalyst was suspended in 100 mL of an aqueous solution containing 1.4 mM coumarin (COUM, 98%, p.a., Alfa Aesar, Ward Hill, MA, USA) that was thermostated (F25/ME, Julabo, Seelbach, Germany) at T = 25 °C. After stirring the suspension at 300 rpm for 20 min in the dark, 30% H_2O_2 (c_0 = 20 mM) was added, and a visible-light lamp (Schott, model KL 2500 LED; an emission spectrum is shown in Figure S11) was used to illuminate the mixture. The intensity of visible-light illumination was quantified using a THORLABS (Newton, NJ, USA) PM400 optical power meter. For the catalytic experiments, the 450 nm LED provided 41 mW cm^{-2}, measured at the point where the incident light enters the reaction chamber and reaches the reaction solution. For the in situ EPR measurements, the illumination intensity was 2.3 mW cm^{-2}, calculated according to the effective beam area restricted by the cavity aperture.

Aqueous-phase samples were taken out at various points during the illumination time and filtered immediately using a 0.2 µm membrane filter (regenerated cellulose). After that, the samples were examined using a UV/Vis photoluminescence spectrometer (Perkin Elmer, model LS 55) using a 10 × 10 mm quartz cuvette to record the photoluminescence signal of the produced 7-OHC. The scanning speed was 200 nm/min, and the wavelength of the excitation light was set to 338 nm. The photoluminescence intensity generated by 7-OHC was measured at around λ = 450 nm [102]. As PL intensity does not directly correspond to •OH radical concentration, we quantified the formation of 7-OHC using a calibration curve obtained from standards measured under identical conditions ($I = 1.42 + 66.46 \times [7\text{-OHC}]$, $R^2 = 0.99993$). This allowed accurate extraction of initial reaction rates from the linear portion of the kinetics and normalization per gram of catalyst and per mole of Cu, enabling meaningful comparison of intrinsic activities across samples.

4. Conclusions

Cu-Fe bimetallic catalysts supported on silica and γ-alumina were successfully synthesized via direct synthesis and an ammonium dawsonite-based route followed by wet impregnation. The results clearly demonstrate that support chemistry plays a decisive role in governing metal dispersion, metal–support interactions, and catalytic stability. γ-alumina promotes highly dispersed Cu and Fe species and stronger metal–support interactions, whereas silica-supported catalysts tend to form CuO aggregates at higher Cu loadings.

Photoluminescence and TCSPC analyses revealed that charge–carrier dynamics and surface-defect states critically determine photo-Fenton performance. In particular, iron was found to exhibit a dual role: low Fe loading facilitates charge separation and enhances photo-Fenton activity, while higher Fe content accelerates electron–hole recombination and suppresses visible-light-driven activity. Catalytic tests using coumarin as a probe molecule confirmed that both the Fe/Cu ratio and the nature of the support govern hydroxyl radical generation and overall catalytic efficiency.

All catalysts exhibited excellent structural stability, with negligible Cu and Fe leaching well below regulatory limits, confirming their suitability for environmentally benign water treatment applications. Overall, this work provides clear design guidelines for efficient heterogeneous photo-Fenton catalysts, emphasizing the need for precise control of metal composition and strong metal–support interactions. While limited photon efficiency under visible-light irradiation remains a challenge, future strategies such as plasmonic coupling or co-catalyst integration may further enhance light utilization.

In summary, the present study offers new mechanistic insights into the interplay between support properties, metal dispersion, and redox synergy, contributing to the rational design of robust and efficient photo-Fenton catalysts for sustainable water treatment.

Supplementary Materials: The following supporting information can be downloaded at: https://www.mdpi.com/article/10.3390/catal16010034/s1.

Author Contributions: N.K.P.: Investigation, methodology, formal analysis, writing—original draft. G.D.: Formal analysis, writing—original draft. A.P.: Conceptualization, investigation, supervision, writing—review and editing, project administration, funding acquisition. N.N.T.: Conceptualization, supervision, writing—review and editing, project administration, funding acquisition. All authors have read and agreed to the published version of the manuscript.

Funding: This research work has received financial support from the Slovenian Research and Innovation Agency (ARIS) in the frame of MSCA COFUND 2023—Seal of Excellence for the PhD program Scientists4Future and research programs P1-0418, P2-0150 and P1-0034.

Data Availability Statement: Data will be made available on request.

Acknowledgments: We sincerely thank Edi Kranjc for conducting the XRD measurements and Mojca Opresnik for performing the SEM-EDX measurements, both from the National Institute of Chemistry, Ljubljana.

Conflicts of Interest: The authors declare that they have no known competing financial interests or personal relationships that could have appeared to influence the work reported in this paper.

References

1. Badea, S.-L.; Niculescu, V.-C. Recent Progress in the Removal of Legacy and Emerging Organic Contaminants from Wastewater Using Metal–Organic Frameworks: An Overview on Adsorption and Catalysis Processes. *Materials* **2022**, *15*, 3850. [CrossRef]
2. Oliveira, T.M.A.; Mansano, A.S.; Holanda, C.A.; Pinto, T.S.; Reis, J.B.; Azevedo, E.B.; Verbinnen, R.T.; Viana, J.L.; Franco, T.C.R.S.; Vieira, E.M. Occurrence and Environmental Risk Assessment of Contaminants of Emerging Concern in Brazilian Surface Waters. *Environ. Toxicol. Chem.* **2024**, *43*, 2199–2210. [CrossRef]
3. Gahrouei, A.E.; Vakili, S.; Zandifar, A.; Pourebrahimi, S. From wastewater to clean water: Recent advances on the removal of metronidazole, ciprofloxacin, and sulfamethoxazole antibiotics from water through adsorption and advanced oxidation processes (AOPs). *Environ. Res.* **2024**, *252*, 119029. [CrossRef]
4. Pandis, P.K.; Kalogirou, C.; Kanellou, E.; Vaitsis, C.; Savvidou, M.G.; Sourkouni, G.; Zorpas, A.A.; Argirusis, C. Key Points of Advanced Oxidation Processes (AOPs) for Wastewater, Organic Pollutants and Pharmaceutical Waste Treatment: A Mini Review. *ChemEngineering* **2022**, *6*, 8. [CrossRef]
5. Parvulescu, V.I.; Epron, F.; Garcia, H.; Granger, P. Recent Progress and Prospects in Catalytic Water Treatment. *Chem. Rev.* **2022**, *122*, 2981–3121. [CrossRef]
6. Ribeiro, J.P.; Nunes, M.I. Recent trends and developments in Fenton processes for industrial wastewater treatment—A critical review. *Environ. Res.* **2021**, *197*, 110957. [CrossRef] [PubMed]
7. Machado, F.; Teixeira, A.C.S.C.; Ruotolo, L.A.M. Critical review of Fenton and photo-Fenton wastewater treatment processes over the last two decades. *Int. J. Environ. Sci. Technol.* **2023**, *20*, 13995–14032. [CrossRef]
8. Lin, Y.; Qiao, J.; Sun, Y.; Dong, H. The profound review of Fenton process: What's the next step? *J. Environ. Sci.* **2025**, *147*, 114–130. [CrossRef]
9. Ziembowicz, S.; Kida, M. Limitations and future directions of application of the Fenton-like process in micropollutants degradation in water and wastewater treatment: A critical review. *Chemosphere* **2022**, *296*, 134041. [CrossRef]
10. Thomas, N.; Dionysiou, D.D.; Pillai, S.C. Heterogeneous Fenton catalysts: A review of recent advances. *J. Hazard. Mater.* **2021**, *404*, 124082. [CrossRef]
11. Vorontsov, A.V. Advancing Fenton and photo-Fenton water treatment through the catalyst design. *J. Hazard. Mater.* **2019**, *372*, 103–112. [CrossRef]
12. Ma, D.; Lai, C.; Yi, H.; Huo, X.; Li, L.; Zhang, M.; Xu, F.; Yan, H.; Hu, S.; Luo, Y. Confinement strategies for the design of efficient heterogeneous Fenton-like catalysts: From nano-space to atomic scale. *Coord. Chem. Rev.* **2025**, *522*, 216241. [CrossRef]
13. Xiao, J.; Guo, S.; Wang, D.; An, Q. Fenton-Like Reaction: Recent Advances and New Trends. *Chem.-Eur. J.* **2024**, *30*, e202304337. [CrossRef]
14. Lin, S.-S.; Gurol, M.D. Catalytic Decomposition of Hydrogen Peroxide on Iron Oxide: Kinetics, Mechanism, and Implications. *Environ. Sci. Technol.* **1998**, *32*, 1417–1423. [CrossRef]
15. Duesterberg, C.K.; Waite, T.D. Process Optimization of Fenton Oxidation Using Kinetic Modeling. *Environ. Sci. Technol.* **2006**, *40*, 4189–4195. [CrossRef]
16. Zhang, M.; Dong, H.; Zhao, L.; Wang, D.; Meng, D. A review on Fenton process for organic wastewater treatment based on optimization perspective. *Sci. Total Environ.* **2019**, *670*, 110–121. [CrossRef]
17. Shang, Y.; Kan, Y.; Xu, X. Stability and regeneration of metal catalytic sites with different sizes in Fenton-like system. *Chin. Chem. Lett.* **2023**, *34*, 108278. [CrossRef]
18. Xu, S.-L.; Wang, W.; Song, Y.; Tang, R.; Hu, Z.-H.; Zhou, X.; Yu, H.-Q. Expanding the pH range of Fenton-like reactions for pollutant degradation: The impact of acidic microenvironments. *Water Res.* **2025**, *270*, 122851. [CrossRef]
19. Cao, G.; Sheng, M.; Niu, W.; Fei, Y.; Li, D. Regeneration and reuse of iron catalyst for Fenton-like reactions. *J. Hazard. Mater.* **2009**, *172*, 1446–1449. [CrossRef]
20. Soufi, A.; Hajjaoui, H.; Boumya, W.; Elmouwahidi, A.; Baillón-García, E.; Abdennouri, M.; Barka, N. Recent trends in magnetic spinel ferrites and their composites as heterogeneous Fenton-like catalysts: A review. *J. Environ. Manag.* **2024**, *367*, 121971. [CrossRef]
21. Jain, B.; Singh, A.K.; Kim, H.; Lichtfouse, E.; Sharma, V.K. Treatment of organic pollutants by homogeneous and heterogeneous Fenton reaction processes. *Environ. Chem. Lett.* **2018**, *16*, 947–967. [CrossRef]

22. Zhu, Y.; Zhu, R.; Xi, Y.; Zhu, J.; Zhu, G.; He, H. Strategies for enhancing the heterogeneous Fenton catalytic reactivity: A review. *Appl. Catal. B* **2019**, *255*, 117739. [CrossRef]
23. Wang, X.; Zhang, X.; Zhang, Y.; Wang, Y.; Sun, S.-P.; Wu, W.D.; Wu, Z. Nanostructured semiconductor supported iron catalysts for heterogeneous photo-Fenton oxidation: A review. *J. Mater. Chem. A* **2020**, *8*, 15513–15546. [CrossRef]
24. Nidheesh, P.V.; Ganiyu, S.O.; Martínez-Huitle, C.A.; Mousset, E.; Olvera-Vargas, H.; Trellu, C.; Zhou, M.; Oturan, M.A. Recent advances in electro-Fenton process and its emerging applications. *Crit. Rev. Environ. Sci. Technol.* **2023**, *53*, 887–913. [CrossRef]
25. Olvera-Vargas, H.; Trellu, C.; Nidheesh, P.V.; Mousset, E.; Ganiyu, S.O.; Martínez-Huitle, C.A.; Zhou, M.; Oturan, M.A. Challenges and opportunities for large-scale applications of the electro-Fenton process. *Water Res.* **2024**, *266*, 122430. [CrossRef]
26. Babuponnusami, A.; Muthukumar, K. A review on Fenton and improvements to the Fenton process for wastewater treatment. *J. Environ. Chem. Eng.* **2014**, *2*, 557–572. [CrossRef]
27. Melero, J.A.; Martínez, F.; Molina, R. Effect of Ultrasound on the Properties of Heterogeneous Catalysts for Sono-Fenton Oxidation Processes. *J. Adv. Oxid. Technol.* **2008**, *11*, 75–83. [CrossRef]
28. Pereira, M.C.; Oliveira, L.C.A.; Murad, E. Iron oxide catalysts: Fenton and Fentonlike reactions—A Review. *Clay Miner.* **2012**, *47*, 285–302. [CrossRef]
29. Zhao, L.; Lin, Z.-R.; Ma, X.; Dong, Y.-H. Catalytic activity of different iron oxides: Insight from pollutant degradation and hydroxyl radical formation in heterogeneous Fenton-like systems. *Chem. Eng. J.* **2018**, *352*, 343–351. [CrossRef]
30. Zhu, Y.; Xie, Q.; Deng, F.; Ni, Z.; Lin, Q.; Cheng, L.; Chen, X.; Qiu, R.; Zhu, R. The differences in heterogeneous Fenton catalytic performance and mechanism of various iron minerals and their influencing factors: A review. *Sep. Purif. Technol.* **2023**, *325*, 124702. [CrossRef]
31. Liu, X.; Yao, Y.; Lu, J.; Zhou, J.; Chen, Q. Catalytic activity and mechanism of typical iron-based catalysts for Fenton-like oxidation. *Chemosphere* **2023**, *311*, 136972. [CrossRef]
32. Liu, Y.; Mao, Y.; Tang, X.; Xu, Y.; Li, C.; Li, F. Synthesis of Ag/AgCl/Fe-S plasmonic catalyst for bisphenol A degradation in heterogeneous photo-Fenton system under visible light irradiation. *Chin. J. Catal.* **2017**, *38*, 1726–1735. [CrossRef]
33. Gogoi, A.; Navgire, M.; Sarma, K.C.; Gogoi, P. Fe_3O_4-CeO_2 metal oxide nanocomposite as a Fenton-like heterogeneous catalyst for degradation of catechol. *Chem. Eng. J.* **2017**, *311*, 153–162. [CrossRef]
34. Choe, Y.J.; Kim, J.; Choi, I.-S.; Kim, S.H. Metal oxides for Fenton reactions toward radical-assisted water treatment: A review. *J. Ind. Eng. Chem.* **2025**, *142*, 127–140. [CrossRef]
35. Yao, Y.; Chen, H.; Qin, J.; Wu, G.; Lian, C.; Zhang, J.; Wang, S. Iron encapsulated in boron and nitrogen codoped carbon nanotubes as synergistic catalysts for Fenton-like reaction. *Water Res.* **2016**, *101*, 281–291. [CrossRef]
36. Wan, Z.; Wang, J. Degradation of sulfamethazine using Fe_3O_4-Mn_3O_4/reduced graphene oxide hybrid as Fenton-like catalyst. *J. Hazard. Mater.* **2017**, *324*, 653–664. [CrossRef]
37. Zubir, N.A.; Yacou, C.; Motuzas, J.; Zhang, X.; Zhao, X.S.; Diniz da Costa, J.C. The sacrificial role of graphene oxide in stabilising a Fenton-like catalyst GO–Fe_3O_4. *Chem. Commun.* **2015**, *51*, 9291–9293. [CrossRef]
38. Wang, L.; Jiang, H.; Wang, H.; Show, P.L.; Ivanets, A.; Luo, D.; Wang, C. MXenes as heterogeneous Fenton-like catalysts for removal of organic pollutants: A review. *J. Environ. Chem. Eng.* **2022**, *10*, 108954. [CrossRef]
39. Ma, J.; Yang, Q.; Wen, Y.; Liu, W. Fe-g-C_3N_4/graphitized mesoporous carbon composite as an effective Fenton-like catalyst in a wide pH range. *Appl. Catal. B* **2017**, *201*, 232–240. [CrossRef]
40. Rahimpour, R.; Chaibakhsh, N.; Zanjanchi, M.A.; Moradi-Shoeili, Z. Fabrication of ZnO/$FeVO_4$ heterojunction nanocomposite with high catalytic activity in photo-Fenton-like process. *J. Alloys Compd.* **2020**, *817*, 152702. [CrossRef]
41. Wang, S.; Zhang, D.; Hu, W.; Li, Y. Efficient generation of singlet oxygen on Fe_2O_3/MoO_3 Z-type heterojunction for removal of ciprofloxacin from water via photo-electro-Fenton-like system. *Chem. Eng. J.* **2024**, *497*, 154400. [CrossRef]
42. Zha, S.; Cheng, Y.; Gao, Y.; Chen, Z.; Megharaj, M.; Naidu, R. Nanoscale zero-valent iron as a catalyst for heterogeneous Fenton oxidation of amoxicillin. *Chem. Eng. J.* **2014**, *255*, 141–148. [CrossRef]
43. Yamaguchi, R.; Kurosu, S.; Suzuki, M.; Kawase, Y. Hydroxyl radical generation by zero-valent iron/Cu (ZVI/Cu) bimetallic catalyst in wastewater treatment: Heterogeneous Fenton/Fenton-like reactions by Fenton reagents formed in-situ under oxic conditions. *Chem. Eng. J.* **2018**, *334*, 1537–1549. [CrossRef]
44. Shah, N.S.; Khan, J.A.; Sayed, M.; Iqbal, J.; Khan, Z.U.H.; Muhammad, N.; Polychronopoulou, K.; Hussain, S.; Imran, M.; Murtaza, B.; et al. Nano-zerovalent copper as a Fenton-like catalyst for the degradation of ciprofloxacin in aqueous solution. *J. Water Proc. Eng.* **2020**, *37*, 101325. [CrossRef]
45. Gao, C.; Chen, S.; Quan, X.; Yu, H.; Zhang, Y. Enhanced Fenton-like catalysis by iron-based metal organic frameworks for degradation of organic pollutants. *J. Catal.* **2017**, *356*, 125–132. [CrossRef]
46. Zhu, Y.; Fan, W.; Feng, W.; Wang, Y.; Liu, S.; Dong, Z.; Li, X. A critical review on metal complexes removal from water using methods based on Fenton-like reactions: Analysis and comparison of methods and mechanisms. *J. Hazard. Mater.* **2021**, *414*, 125517. [CrossRef]

47. Chen, D.; Chen, S.; Jiang, Y.; Xie, S.; Quan, H.; Hua, L.; Luo, X.; Guo, L. Heterogeneous Fenton-like catalysis of Fe-MOF derived magnetic carbon nanocomposites for degradation of 4-nitrophenol. *RSC Adv.* **2017**, *7*, 49024–49030. [CrossRef]
48. Tang, J.; Wang, J. MOF-derived three-dimensional flower-like FeCu@C composite as an efficient Fenton-like catalyst for sulfamethazine degradation. *Chem. Eng. J.* **2019**, *375*, 122007. [CrossRef]
49. Lyu, L.; Yu, G.; Zhang, L.; Hu, C.; Sun, Y. 4-Phenoxyphenol-Functionalized Reduced Graphene Oxide Nanosheets: A Metal-Free Fenton-Like Catalyst for Pollutant Destruction. *Environ. Sci. Technol.* **2018**, *52*, 747–756. [CrossRef]
50. Bokare, A.D.; Choi, W. Review of iron-free Fenton-like systems for activating H_2O_2 in advanced oxidation processes. *J. Hazard. Mater.* **2014**, *275*, 121–135. [CrossRef]
51. Garrido-Ramírez, E.G.; Theng, B.K.G.; Mora, M.L. Clays and oxide minerals as catalysts and nanocatalysts in Fenton-like reactions—A review. *Appl. Clay Sci.* **2010**, *47*, 182–192. [CrossRef]
52. Shokri, A.; Fard, M.S. A critical review in Fenton-like approach for the removal of pollutants in the aqueous environment. *Environ. Chall.* **2022**, *7*, 100534. [CrossRef]
53. Liu, Y.; Wang, J. Multivalent metal catalysts in Fenton/Fenton-like oxidation system: A critical review. *Chem. Eng. J.* **2023**, *466*, 143147. [CrossRef]
54. Gutierrez-Mata, A.G.; Velazquez-Martínez, S.; Álvarez-Gallegos, A.; Ahmadi, M.; Hernández-Pérez, J.A.; Ghanbari, F.; Silva-Martínez, S. Recent Overview of Solar Photocatalysis and Solar Photo-Fenton Processes for Wastewater Treatment. *Int. J. Photoenergy* **2017**, *2017*, 8528063. [CrossRef]
55. Ameta, R.; Chohadia, A.K.; Jain, A.; Punjabi, P.B. Fenton and Photo-Fenton Processes. In *Advanced Oxidation Processes for Waste Water Treatment*; Elsevier: Amsterdam, The Netherlands, 2018; pp. 49–87. [CrossRef]
56. Ali, H.M.; Roghabadi, F.A.; Ahmadi, V. Solid-supported photocatalysts for wastewater treatment: Supports contribution in the photocatalysis process. *J. Sol. Energy* **2023**, *255*, 99–125. [CrossRef]
57. Ullah, S.; Ferreira-Neto, E.P.; Khan, A.A.; Medeiros, I.P.M.; Wender, H. Supported nanostructured photocatalysts: The role of support-photocatalyst interactions. *Photochem. Photobiol. Sci.* **2022**, *22*, 219–240. [CrossRef] [PubMed]
58. Šuligoj, A.; Ristić, A.; Dražić, G.; Pintar, A.; Zabukovec Logar, N.; Novak Tušar, N. Bimetal Cu-Mn porous silica-supported catalyst for Fenton-like degradation of organic dyes in wastewater at neutral pH. *Catal. Today* **2020**, *358*, 270–277. [CrossRef]
59. Farhadian, N.; Liu, S.; Asadi, A.; Shahlaei, M.; Moradi, S. Enhanced heterogeneous Fenton oxidation of organic pollutant via Fe-containing mesoporous silica composites: A review. *J. Mol. Liq.* **2021**, *321*, 114896. [CrossRef]
60. Stoica, G. Chemistry of Dawsonites and Application in Catalysis. Ph.D. Thesis, Universitat Rovira i Virgili, Tarragona, Spain, 2010.
61. Ali, A.A.; Hasan, M.A.; Zaki, M.I. Dawsonite-Type Precursors for Catalytic Al, Cr, and Fe Oxides: Synthesis and Characterization. *Chem. Mater.* **2005**, *17*, 6797–6804. [CrossRef]
62. Hu, X.; Liu, Y.; Tang, Z.; Li, G.; Zhao, R.; Liu, C. Fabrication of high-surface-area γ-alumina by thermal decomposition of AACH precursor using low-temperature solid-state reaction. *Mater. Res. Bull.* **2012**, *47*, 4271–4277. [CrossRef]
63. Djinović, P.; Ristić, A.; Žumbar, T.; Dasireddy, V.D.B.C.; Rangus, M.; Dražić, G.; Popova, M.; Likozar, B.; Zabukovec Logar, N.; Novak Tušar, N. Synergistic effect of CuO nanocrystals and Cu-oxo-Fe clusters on silica support in promotion of total catalytic oxidation of toluene as a model volatile organic air pollutant. *Appl. Catal. B* **2020**, *268*, 118749. [CrossRef]
64. Žumbar, T.; Arčon, I.; Djinović, P.; Aquilanti, G.; Žerjav, G.; Pintar, A.; Ristić, A.; Dražić, G.; Volavšek, J.; Mali, G.; et al. Winning Combination of Cu and Fe Oxide Clusters with an Alumina Support for Low-Temperature Catalytic Oxidation of Volatile Organic Compounds. *ACS Appl. Mater. Interfaces* **2023**, *15*, 28747–28762. [CrossRef] [PubMed]
65. Misra, M.; Chowdhury, S.R.; Il Lee, T. Sunlight driven decomposition of toxic organic compound, coumarin, p-nitrophenol, and photo reduction of Cr(VI) ions, using a bridge structure of Au@CNT@TiO_2 nanocomposite. *Appl. Catal. B* **2020**, *272*, 118991. [CrossRef]
66. Wang, J.; Liu, C.; Tong, L.; Li, J.; Luo, R.; Qi, J.; Li, Y.; Wang, L. Iron–copper bimetallic nanoparticles supported on hollow mesoporous silica spheres: An effective heterogeneous Fenton catalyst for orange II degradation. *RSC Adv.* **2015**, *5*, 69593–69605. [CrossRef]
67. Huang, Z.; Chen, Z.; Chen, Y.; Hu, Y. Synergistic effects in iron-copper bimetal doped mesoporous γ-Al_2O_3 for Fenton-like oxidation of 4-chlorophenol: Structure, composition, electrochemical behaviors and catalytic performance. *Chemosphere* **2018**, *203*, 442–449. [CrossRef]
68. Thommes, M.; Kaneko, K.; Neimark, A.V.; Olivier, J.P.; Rodriguez-Reinoso, F.; Rouquerol, J.; Sing, K.S.W. Physisorption of gases, with special reference to the evaluation of surface area and pore size distribution (IUPAC Technical Report). *Pure Appl. Chem.* **2015**, *87*, 1051–1069. [CrossRef]
69. Fu, L.; Yang, H. Tailoring the Electronic Structure of Mesoporous Spinel γ-Al_2O_3 at Atomic Level: Cu-Doped Case. *J. Phys. Chem. C* **2014**, *118*, 14299–14315. [CrossRef]
70. Aalim, M.; Shah, M.A. Role of oxygen vacancies and porosity in enhancing the electrochemical properties of Microwave synthesized hematite (α-Fe_2O_3) nanostructures for supercapacitor application. *Vacuum* **2023**, *210*, 111903. [CrossRef]
71. Boccuzzi, F.; Coluccia, S.; Martra, G.; Ravasio, N. Cu/SiO_2 and Cu/SiO_2–TiO_2 Catalysts. *J. Catal.* **1999**, *184*, 316–326. [CrossRef]

72. Guerra-Que, Z.; Pérez-Vidal, H.; Torres-Torres, G.; Arévalo-Pérez, J.C.; Silahua Pavón, A.A.; Cervantes-Uribe, A.; Espinosa de los Monteros, A.; Lunagómez-Rocha, M.A. Treatment of phenol by catalytic wet air oxidation: A comparative study of copper and nickel supported on γ-alumina, ceria and γ-alumina–ceria. *RSC Adv.* **2019**, *9*, 8463–8479. [CrossRef]
73. Pérez-Ramírez, J.; Santhosh Kumar, M.; Brückner, A. Reduction of N_2O with CO over FeMFI zeolites: Influence of the preparation method on the iron species and catalytic behavior. *J. Catal.* **2004**, *223*, 13–27. [CrossRef]
74. Wahiduzzaman, M.; Wang, S.; Schnee, J.; Vimont, A.; Ortiz, V.; Yot, P.G.; Retoux, R.; Daturi, M.; Lee, J.S.; Chang, J.-S.; et al. A High Proton Conductive Hydrogen-Sulfate Decorated Titanium Carboxylate Metal−Organic Framework. *ACS Sustain. Chem. Eng.* **2019**, *7*, 5776–5783. [CrossRef]
75. Žumbar, T.; Ristić, A.; Dražić, G.; Lazarova, H.; Volavšek, J.; Pintar, A.; Zabukovec Logar, N.; Novak Tušar, N. Influence of Alumina Precursor Properties on Cu-Fe Alumina Supported Catalysts for Total Toluene Oxidation as a Model Volatile Organic Air Pollutant. *Catalysts* **2021**, *11*, 252. [CrossRef]
76. Tsaturyan, A.A.; Cherkasova, S.O.; Budnyk, A.P. Theoretical and experimental characterization of Cu-doped amorphous silicate glass. *J. Mol. Struct.* **2020**, *1205*, 127629. [CrossRef]
77. Fu, L.; Li, X.; Liu, M.; Yang, H. Insights into the nature of Cu doping in amorphous mesoporous alumina. *J. Mater. Chem. A* **2013**, *1*, 14592. [CrossRef]
78. Baronskiy, M.; Rastorguev, A.; Zhuzhgov, A.; Kostyukov, A.; Krivoruchko, O.; Snytnikov, V. Photoluminescence and Raman spectroscopy studies of low-temperature γ-Al_2O_3 phases synthesized from different precursors. *Opt. Mater.* **2016**, *53*, 87–93. [CrossRef]
79. Baraban, A.P.; Samarin, S.N.; Prokofiev, V.A.; Dmitriev, V.A.; Selivanov, A.A.; Petrov, Y. Luminescence of SiO_2 layers on silicon at various types of excitation. *J. Lumin.* **2019**, *205*, 102–108. [CrossRef]
80. Fujimoto, Y.; Nakatsuka, M. Spectroscopic properties and quantum yield of Cu-doped SiO_2 glass. *J. Lumin.* **1997**, *75*, 213–219. [CrossRef]
81. Jitianu, A.; Crisan, M.; Meghea, A.; Rau, I.; Zaharescu, M. Influence of the silica based matrix on the formation of iron oxide nanoparticles in the Fe_2O_3–SiO_2 system, obtained by sol–gel method. *J. Mater. Chem.* **2002**, *12*, 1401–1407. [CrossRef]
82. Piazzesi, G.; Nicosia, D.; Devadas, M.; Kröcher, O.; Elsener, M.; Wokaun, A. Investigation of HNCO adsorption and hydrolysis on Fe-ZSM5. *Catal. Lett.* **2007**, *115*, 33–39. [CrossRef]
83. Gervasini, A.; Manzoli, M.; Martra, G.; Ponti, A.; Ravasio, N.; Sordelli, L.; Zaccheria, F. Dependence of Copper Species on the Nature of the Support for Dispersed CuO Catalysts. *J. Phys. Chem. B* **2006**, *110*, 7851–7861. [CrossRef]
84. Wang, Z.; Liu, Q.; Yu, J.; Wu, T.; Wang, G. Surface structure and catalytic behavior of silica-supported copper catalysts prepared by impregnation and sol–gel methods. *Appl. Catal. A* **2003**, *239*, 87–94. [CrossRef]
85. Zhu, W.; Wang, L.; Liu, S.; Wang, Z. Characterization and catalytic behavior of silica-supported copper catalysts prepared by impregnation and ion-exchange methods. *React. Kinet. Catal. Lett.* **2008**, *93*, 93–99. [CrossRef]
86. Garcia, C.L.; Resasco, D.E. Effects of the support and the addition of a second promoter on potassium chloride-copper(II) chloride catalysts used in the oxychlorination of methane. *Appl. Catal.* **1989**, *46*, 251–267. [CrossRef]
87. Leandri, V.; Gardner, J.M.; Jonsson, M. Coumarin as a Quantitative Probe for Hydroxyl Radical Formation in Heterogeneous Photocatalysis. *J. Phys. Chem. C* **2019**, *123*, 6667–6674. [CrossRef]
88. Žerjav, G.; Albreht, A.; Vovk, I.; Pintar, A. Revisiting terephthalic acid and coumarin as probes for photoluminescent determination of hydroxyl radical formation rate in heterogeneous photocatalysis. *Appl. Catal. A* **2020**, *598*, 117566. [CrossRef]
89. Garcia-Segura, S.; Brillas, E.; Cornejo-Ponce, L.; Salazar, R. Effect of the Fe^{3+}/Cu^{2+} ratio on the removal of the recalcitrant oxalic and oxamic acids by electro-Fenton and solar photoelectro-Fenton. *Sol. Energy* **2016**, *124*, 242–253. [CrossRef]
90. Salazar, R.; Brillas, E.; Sirés, I. Finding the best Fe^{2+}/Cu^{2+} combination for the solar photoelectro-Fenton treatment of simulated wastewater containing the industrial textile dye Disperse Blue 3. *Appl. Catal. B* **2012**, *115–116*, 107–116. [CrossRef]
91. Vidruk, R.; Landau, M.V.; Herskowitz, M.; Ezersky, V.; Goldbourt, A. Control of surface acidity and catalytic activity of γ-Al_2O_3 by adjusting the nanocrystalline contact interface. *J. Catal.* **2011**, *282*, 215–227. [CrossRef]
92. Bai, P.; Ma, Z.; Li, T.; Tian, Y.; Zhang, Z.; Zhong, Z.; Xing, W.; Wu, P.; Liu, X.; Yan, Z. Relationship between Surface Chemistry and Catalytic Performance of Mesoporous γ-Al_2O_3 Supported VO_x Catalyst in Catalytic Dehydrogenation of Propane. *ACS Appl. Mater. Interfaces* **2016**, *8*, 25979–25990. [CrossRef]
93. Subramanian, P.; Meziane, D.; Wojcieszak, R.; Dumeignil, F.; Boukherroub, R.; Szunerits, S. Plasmon-Induced Electrocatalysis with Multi-Component Nanostructures. *Materials* **2018**, *12*, 43. [CrossRef] [PubMed]
94. Periyasamy, M.; Sain, S.; Sengupta, U.; Mandal, M.; Mukhopadhyay, S.; Kar, A. Bandgap tuning of photo Fenton-like Fe_3O_4/C catalyst through oxygen vacancies for advanced visible light photocatalysis. *Mater. Adv.* **2021**, *2*, 4843–4858. [CrossRef]
95. Novak Tušar, N.; Maučec, D.; Rangus, M.; Arčon, I.; Mazaj, M.; Cotman, M.; Pintar, A.; Kaučič, V. Manganese Functionalized Silicate Nanoparticles as a Fenton-Type Catalyst for Water Purification by Advanced Oxidation Processes (AOP). *Adv. Funct. Mater.* **2012**, *22*, 820–826. [CrossRef]

96. Laffircher, R.; Digne, M.; Salvatori, F.; Boualleg, M.; Colson, D.; Puel, F. Ammonium aluminium carbonate hydroxide $NH_4Al(OH)_2CO_3$ as an alternative route for alumina preparation: Comparison with the classical boehmite precursor. *Powder Technol.* **2017**, *320*, 565–573. [CrossRef]
97. Laffitcher, R.; Digne, M.; Salvatori, F.; Boualleg, M.; Colson, D.; Puel, F. Development of new alumina precipitation routes for catalysis applications. *J. Cryst. Growth* **2017**, *468*, 526–530. [CrossRef]
98. Brunauer, S.; Emmett, P.H.; Teller, E. Adsorption of Gases in Multimolecular Layers. *J. Am. Chem. Soc.* **1938**, *60*, 309–319. [CrossRef]
99. Zepeda, T.A.; Fierro, J.L.G.; Pawelec, B.; Nava, R.; Klimova, T.; Fuentes, G.A.; Halachev, T. Synthesis and Characterization of Ti-HMS and CoMo/Ti-HMS Oxide Materials with Varying Ti Content. *Chem. Mater.* **2005**, *17*, 4062–4073. [CrossRef]
100. Barrett, E.P.; Joyner, L.G.; Halenda, P.P. The Determination of Pore Volume and Area Distributions in Porous Substances. I. Computations from Nitrogen Isotherms. *J. Am. Chem. Soc.* **1951**, *73*, 373–380. [CrossRef]
101. Šuligoj, A.; Trendafilova, I.; Maver, K.; Pintar, A.; Ristić, A.; Dražić, G.; Abdelraheem, W.H.M.; Jagličić, Z.; Arčon, I.; Zabukovec Logar, N.; et al. Multicomponent Cu–Mn–Fe silica supported catalysts to stimulate photo-Fenton-like water treatment under sunlight. *J. Environ. Chem. Eng.* **2023**, *11*, 110369. [CrossRef]
102. Louit, G.; Foley, S.; Cabillic, J.; Coffigny, H.; Taran, F.; Valleix, A.; Renault, J.P.; Pin, S. The reaction of coumarin with the OH radical revisited: Hydroxylation product analysis determined by fluorescence and chromatography. *Radiat. Phys. Chem.* **2005**, *72*, 119–124. [CrossRef]